J. Mech. Phys. Solids 99 (2017) 70–92

Contents lists available at ScienceDirect

Journal of the Mechanics and Physics of Solids

journal homepage: www.elsevier.com/locate/jmps

Compression testing spherical particles for strength: Theory of the meridian crack test and implementation for microscopic fused quartz

Václav Pejchal*, Goran Žagar, Raphaël Charvet, Cyril Dénéréaz, Andreas Mortensen

Laboratory of Mechanical Metallurgy, Institute of Materials, École Polytechnique Fédérale de Lausanne (EPFL), Station 12, CH-1015 Lausanne, Switzerland

ARTICLE INFO

Keywords:
Uniaxial compression
Powder particles
Fused quartz
Local strength
Survival-analysis

ABSTRACT

We show that uniaxial compression testing of spherical particles can give unambiguous access to their tensile strength as governed by surface flaws if one uses pairs of elasto-plastic platens, tailoring their hardness in order to control the relative area of particle-to-platen contact during the test. This eliminates the development of contact microcracks that are typically found to govern particle fracture when hard platens are used. We show that, if the platen materials are well chosen, one can probe a range of stress states for which it is known that particle failure was initiated along the surface, under elevated hoop stress within a region situated remote from the points of load application. Specifically, platens must be chosen such that particles tend to fracture when the ratio of projected contact area radius to particle radius exceeds a specific value that depends on the Poisson ratio of the particles. With fused quartz of Poisson ratio 0.17, this specific ratio value equals 0.65. We demonstrate the approach using microscopic fused quartz spheres 40 ± 20 μm in diameter as a testbench material; with those particles hardened steel serves as an appropriate platen material. Their strength values are statistically distributed; this is addressed using several platen materials. The resulting bank of data is interpreted using established survival-analysis methods, namely the non-parametric product-limit estimator. We also give a maximum likelihood estimation of the particle strength Weibull distribution parameters derived from the ensemble of data after left-truncation and/or right-censoring of data points situated inside of the range of unambiguous surface fracture strength measurement for each platen material. This gives a Weibull modulus of 6.3 and characteristic strength of 890 MPa for the fused quartz particles. These values are significantly lower than what is produced in high-strength fused quartz fibers of comparable diameter; the difference is most likely a result of surface damage caused during powder storage and manipulation in the absence of a protective coating.

1. Introduction

The strength of brittle particles is important in many different fields of science or engineering. The strength of rock and mineral particles dictates the energy consumed in mining processes (Broch and Franklin, 1972). Particle strength also governs the mechanical behavior of many soils (Brzesowsky et al., 2011; McDowell and Bolton, 1998; Nakata et al., 1999) and is an important

* Corresponding author.
E-mail address: vaclav.pejchal@epfl.ch (V. Pejchal).

http://dx.doi.org/10.1016/j.jmps.2016.11.009
Received 8 July 2016; Received in revised form 2 November 2016; Accepted 15 November 2016
Available online 17 November 2016
0022-5096/ © 2016 The Authors. Published by Elsevier Ltd.
This is an open access article under the CC BY license (http://creativecommons.org/licenses/BY/4.0/).

parameter in processes of powder granulation and compaction, which are present across a wide range of industries (including for example food and pharmaceutical industries) (Antonyuk et al., 2010, 2005; Khanal et al., 2008; Yap et al., 2008, 2006). In materials processing the strength of particles governs grinding (Lobo-Guerrero and Vallejo, 2006) and comminution processes and also the processing of ceramics (Tavares, 2007). In addition, the mechanical behavior of a wide range of composite materials, alloys or concrete, is governed by the strength of the microscopic particulate phases that they contain (Gammage et al., 2004; Hauert et al., 2009; Khanal et al., 2008; Miserez and Mortensen, 2004).

There is at present no well-established method to measure the strength of individual particles. Cutting out beam-like test specimens from the particle is generally impractical and might also lead to irrelevant result, since practically any cutting or machining procedure may introduce extraneous flaws (Kiener et al., 2007; Rice, 1979; Shim et al., 2009). Rather, the most common method used to measure the strength of individual particles is to compress the whole particle until it breaks. Two methods are generally used to this end. One is to impact accelerated particles against a hard substrate and record the velocity at which the particles break (Chau et al., 2000; Dean et al., 1952). The other is the quasi-static, uniaxial compression test, in which a particle is compressed between two parallel platens until it fails, recording the load and platen displacement during the test. The reason why both tests can generate meaningful strength measurements in brittle particles is that the stress distributions that they produce within the particle are so inhomogeneous that tension is often produced somewhere within the compressed particle.

For tractability, equiaxed particles are often assimilated to spheres in compression test data analysis. The solution for the stress field that is created within a sphere when it is compressed uniaxially across two points situated at either end of a diameter is well known; a frequently used treatment is that of Hiramatsu and Oka (Hiramatsu and Oka, 1967, 1966). These authors analyzed the stress within an isotropic linear elastic sphere of radius R compressed by a pair of uniformly distributed radial loads acting symmetrically over two equal spherical caps centered along the compression axis and of outer circle defining the *contact radius*, a. For (a/R) =0.04 to 0.13, Hiramatsu and Oka showed that the peak tensile stress is located along the compression axis, and is roughly equal to ~0.7 times the *nominal stress*, defined as $F/\pi R^2$, where F is the load acting on each spherical cap. This conclusion has been debated, notably because, depending on the precise value of a/R, the peak value of the tensile stress along the compression axis can deviate significantly from 0.7 (Darvell, 1990; Hiramatsu and Oka, 1967; Salençon, 1966; Wijk, 1978).

Following Hiramatsu and Oka's analysis, the “tensile strength” of particles tested in uniaxial compression is therefore often computed as:

$$\sigma_T = \kappa \frac{F_f}{\pi R^2}, \tag{1}$$

where F_f is the peak (failure) load and κ is a constant near unity. Experimental data of Jaeger (Jaeger, 1967) and analysis by several authors suggest that $0.7 \le \kappa \le 1.4$. Many experimental studies have used this expression to evaluate the strength of spherical or irregular particles tested in uniaxial compression (McDowell and Amon, 2000; McDowell and Bolton, 1998; Nakata et al., 1999; Ogiso et al., 2007; Pitchumani et al., 2004; Portnikov et al., 2013; Ribas et al., 2014; Rozenblat et al., 2011; Verrall, 1976; Yap et al., 2008, 2006; Yoshida et al., 2005; Zhao et al., 2013).

In nearly all uniaxial particle compression tests to date, platens are used that are much harder than the particle, such that $(a/R) \le 0.1$. This is convenient from a practical point of view, because the particle will then not damage the platens. Also, Hertzian contact theory can then be used to calculate a/R (Huang et al., 2014) and the stress state is relatively well defined, with its peak tensile value given by Eq. (1) and reached along the particle diameter parallel to the compression axis, generally near the load application points and with $\kappa \ge 1$. There are, though, disadvantages to the use of hard platens. First, when a particle is compressed between two platens much harder than itself, the high stress concentration that develops at and near the small area of contact between the platens and the particle can cause the nucleation of extraneous cracks that may then govern the measured particle fracture stress, obscuring the detection of intrinsic particle flaws (Khanal et al., 2008; Majzoub and Chaudhri, 2000; Schönert, 2004; Swab et al., 2011). Moreover, in many strong brittle particles, the largest defects are located not within the particle, but along its surface (Lawn, 1993), which is at best poorly sampled when the site of peak tensile stress is located, not at the surface, but deep within the particle.

Those limitations, and a solution thereto, were identified by Shipway and Hutchings in a 1993 contribution that we consider to be a significant, but so far underexploited, advance in the state of the art of particle testing (Shipway and Hutchings, 1993a, 1993b). These authors reanalyzed the particle stress field solution for the problem of compression of a linearly elastic sphere compressed by symmetric pressure uniformly distributed over the surface of the spherical caps at either end of a diameter. They pointed out that there can be a significant tensile hoop stress, σ_ϕ acting along the equatorial belt of the particle surface, due to which the particle could fail. Over the range $0 \le (a/R) \le 0.8$ this tensile hoop stress remains roughly equal to

$$\sigma_\phi \approx 0.4 \frac{F}{\pi R^2}. \tag{2}$$

In addition, Shipway and Hutchings showed that as the ratio a/R increases, i.e., if the particle is allowed to sink more deeply into the platen material, then the location of the peak tensile stress shifts from the compression axis to the equatorial belt region. For a material with Poisson's ratio ν=0.25, this transition happens when $(a/R) \approx 0.6$. Past that point, the hoop tensile stress σ_ϕ in the equatorial belt exceeds the tensile stress anywhere else within the spherical particle.

Shipway and Hutchings also put their conclusions to practice, testing spheres, roughly 700–800 μm in diameter, of lead glass or sapphire using a variety of platen materials. They showed that more consistent particle strength values are obtained using Eq. (2) as compared to Eq. (1), implying that fracture was more likely initiated from the particle surface than from its interior.

At the microscopic and nano- scales quasi-static uniaxial compression tests become even more challenging. There are only a few

articles in which particles of diameter having order of magnitude 10 μm or below have been tested in uniaxial compression to produce meaningful strength data; examples are in (Gerberich et al., 2003; Mook et al., 2007; Ogiso et al., 2007; Ribas et al., 2014; Romeis et al., 2012; Yap et al., 2006; Yoshida et al., 2005). Such particles are typically compressed between a flat-ended nanoindentor diamond tip and a very hard base platen, such that fracture initiation caused by the platen has to be considered in data interpretation (Chaudhri, 2004; Majzoub and Chaudhri, 2000; Mook et al., 2007). This led in one study to back-calculated flaw sizes that were 1–3 orders of magnitude smaller than the flaws observed by microscopy (Brzesowsky et al., 2011).

In the work presented here we extend the approach of Shipway and Hutchings to present a testing approach in which a collection of elasto-plastic platens of tailored hardness are used to generate series of data from which the statistically distributed strength of small glass spheres ~40 μm diameter can be measured and interpreted using the methodology of survival analysis. We deliberately tailor the hardness of the platens to produce fracture events past (a/R) =0.65, a region of relative contact radii that was not explored by Shipway and Hutchings. We use a custom-built instrumented crushing apparatus designed to work in displacement-controlled mode, which features a stiff load-train so as to ease fractography. Using analytical solutions for the stress distribution within the particle, we show how this modification of the crushing test can produce unambiguous measurements of the intrinsic tensile strength distribution of strong brittle microscopic particles.

2. Theory

Consider the compression of a brittle elastic spherical particle of radius R between a pair of soft (relatively to the particle) elasto-plastic platens under an applied force F (Fig. 1a). As the platens compress the particle, they deform plastically, producing an indent of contact radius a. As particle compression continues, a gradually increases with increasing applied compressive force F. We neglect the effect of friction between the platens and the compressed particle and assume that the compressive force is uniformly distributed over the spherical cap as pressure $q=F/A$. Any material pile-up arising from the indentation of the platen is accounted for via the contact radius a. The cap has an area $A=2\pi Rh$ where h is the contact depth (Fig. 1b). This is the boundary value problem analyzed by Hiramatsu and Oka, or Shipway and Hutchings (HO-SH).

The HO-SH analysis is conveniently carried out in the spherical coordinate system having its origin placed in the center of the sphere and variables being the radial distance r, the polar angle θ, and the azimuthal angle ϕ. Due to spherical symmetry, for given F, R and A (related to the contact radius a, see Fig. 1b), the stress field in the sphere has four independent components:

$$\sigma_r = \frac{F}{\pi R^2}\bullet\tilde{\sigma}_r\left(\frac{a}{R}, \frac{r}{R}, \theta, \nu\right), \tag{3a}$$

$$\sigma_\theta = \frac{F}{\pi R^2}\bullet\tilde{\sigma}_\theta\left(\frac{a}{R}, \frac{r}{R}, \theta, \nu\right), \tag{3b}$$

$$\sigma_\phi = \frac{F}{\pi R^2}\bullet\tilde{\sigma}_\phi\left(\frac{a}{R}, \frac{r}{R}, \theta, \nu\right), \tag{3c}$$

$$\tau_{r\theta} = \frac{F}{\pi R^2}\bullet\tilde{\tau}_{r\theta}\left(\frac{a}{R}, \frac{r}{R}, \theta, \nu\right), \tag{3d}$$

In Eqs. (3a-d), $\tilde{\sigma}_r$, $\tilde{\sigma}_\theta$, $\tilde{\sigma}_\phi$ and $\tilde{\tau}_{r\theta}$ are the normalized components of the local stress tensor; these are given in Appendix A. Note that, besides the geometrical parameters, the stress field given by Eqs. (3a-d) explicitly depends also on the Poisson's ratio, ν, of the sphere material.

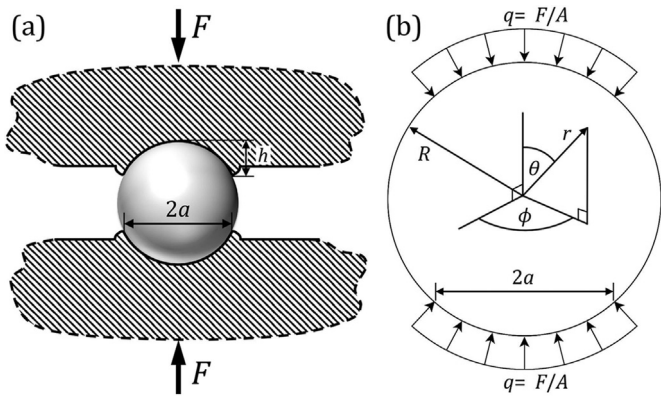

Fig. 1. (a) Sketch of a spherical particle of radius R compressed between two elasto-plastic platens under load F. (b) Simplified boundary value problem associated with the sketch in (a). Pressure distribution in the region of contact, i.e. over the area of the spherical cap defined by the contact radius a and contact depth h, is assumed to be uniform: shear contact forces arising from friction and variations in normal stress are neglected. Possible pile-up of the platen material due to indentation is assumed comprised via the contact radius definition.

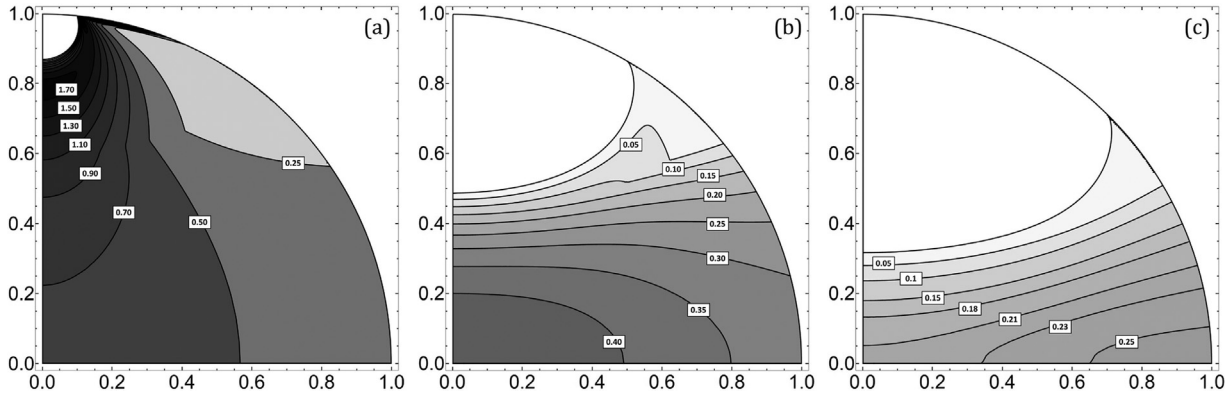

Fig. 2. Distribution of the positive (tensile) normalized first principal stress, $\tilde{\sigma}_1 = \sigma_1 \pi R^2/F$, calculated by solving Eq. (4), for relative contact radius values (a/R) =0.1 (a), 0.5 (b) and 0.7 (c). Regions of the sphere where $\tilde{\sigma}_1$ is negative (i.e., compressive) are shown in white. Poisson's ratio of the sphere is taken as ν=0.17, typical of glass. Given spherical symmetry only one quarter of the $\{r, \theta\}$–plane is considered. The axes represent normalized radial distance r/R.

The quantity of interest in brittle fracture is the first principal stress field, $\tilde{\sigma}_1(\frac{a}{R}, \frac{r}{R}, \theta, \nu)$, and this, for a spherical particle, can be computed from Eqs. (3a-d) by solving the eigenvalue problem defined by the local stress tensor,

$$\det\left(\begin{bmatrix} \tilde{\sigma}_r - \lambda_i & \tilde{\tau}_{r\theta} & 0 \\ \tilde{\tau}_{r\theta} & \tilde{\sigma}_\theta - \lambda_i & 0 \\ 0 & 0 & \tilde{\sigma}_\phi - \lambda_i \end{bmatrix}\right) = 0, \tag{4}$$

such that $\tilde{\sigma}_1(\frac{a}{R}, \frac{r}{R}, \theta, \nu) = \max\{\lambda_i(\frac{a}{R}, \frac{r}{R}, \theta, \nu)\}$ for all points within the sphere. By symmetry, the first principal stress everywhere along the compression axis is $\tilde{\sigma}_\theta = \tilde{\sigma}_\phi$. On the surface along the equatorial line and at sufficiently large distance away from the contact perimeter the first principal stress corresponds to $\tilde{\sigma}_\phi$.

The first principal stress fields, $\tilde{\sigma}_1 = \sigma_1 \pi R^2/F$, calculated via Eq. (4) for relative contact radius values (a/R) =0.1, 0.5 and 0.7 and a Poisson's ratio ν=0.17 (typical of quartz and glass) are shown in Fig. 2. In Fig. 2 we plot only the positive, i.e. tensile values of the $\tilde{\sigma}_1$-field (indicated by the grey scale) since only those regions are potentially interesting for the Mode I failure of a brittle material. In Fig. 3 we directly plot the values of the first principal stress in the sphere center, $\tilde{\sigma}_{1c} = \tilde{\sigma}_1(r = 0, \theta = 0)$ and along the equatorial line, $\tilde{\sigma}_{1s} = \tilde{\sigma}_1(r = R, \theta = \frac{\pi}{2})$, versus a/R, along with the value for the global maximum of the $\tilde{\sigma}_1$–field. From Figs. 2 and 3 it is evident that the $\tilde{\sigma}_1$-field distribution is very sensitive to a/R. For low a/R, up to 0.3, $\tilde{\sigma}_1$ is highly concentrated just outside the contact perimeter over which the load is applied and/or along the loading axis; in those locations it is oriented along the θ direction, $\tilde{\sigma}_1 = \tilde{\sigma}_\theta$ (Fig. 2a). At intermediate contact radii, $0.3 < (a/R) < 0.65$, the highest values of $\tilde{\sigma}_1$ are found away from the contact, deeper within the sphere with the peak value located near the sphere center (Fig. 2b). Finally, for $(a/R) > 0.65$ (Fig. 2c), the region of highest tensile stress $\tilde{\sigma}_1$ is shifted towards the sphere surface: the peak tensile stress within the particle is now situated along the sphere equator and is a hoop stress, $\tilde{\sigma}_1 = \tilde{\sigma}_\phi$.

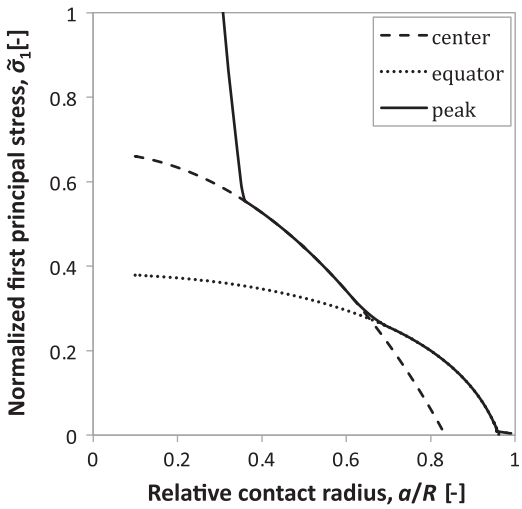

Fig. 3. Normalized first principal stress $\tilde{\sigma}_1 = \sigma_1 \pi R^2/F$ vs. the relative contact radius a/R , obtained by solving Eq. (4), in the center of the sphere $\tilde{\sigma}_{1c} = \tilde{\sigma}_1(r = 0, \theta = 0)$ (dashed line) and on the surface equator $\tilde{\sigma}_{1s} = \tilde{\sigma}_1(r = R, \theta = \frac{\pi}{2})$(dotted line). The value of the global maximum, $\max(\tilde{\sigma}_1)$,is shown with the solid line. Poisson's ratio of the sphere is taken as ν=0.17, typical of glass.

Consider a particle that is gradually compressed between a pair of defined metallic platens. As the load increases, the particle gradually indents the platens. If we assume that, when pressed against the deforming metal platens, the hard particle behaves as if it were rigid, then the relation linking $F/\pi R^2$ with a/R is entirely dictated by the platen material deformation law. This behavior is known to be described, for fully plastic deformation of the platen material, by the empirical Meyer law classically used in the interpretation of hardness tests (Tabor, 1951):

$$\frac{F}{\pi R^2} = k\left(\frac{a}{R}\right)^n, \tag{5}$$

where k and n are characteristic of the indented material. The exponent n varies typically from 2 (typical of fully strain-hardened metals) to 2.5 (typical of fully annealed metals) and coefficient k is associated with the material hardness (Dieter, 1986; Tabor, 1951).

Inserting Meyer's law, Eq. (5), into the HO-SH solution given by Eqs. (3a-d), one obtains the following expressions for the dimensionless stress field components within a sphere compressed by a pair of symmetric elasto-plastic platens,

$$\frac{\sigma_r}{k} = \left(\frac{a}{R}\right)^n \bullet \tilde{\sigma}_r\left(\frac{a}{R}, \frac{r}{R}, \theta, \nu\right), \tag{6a}$$

$$\frac{\sigma_\theta}{k} = \left(\frac{a}{R}\right)^n \bullet \tilde{\sigma}_\theta\left(\frac{a}{R}, \frac{r}{R}, \theta, \nu\right), \tag{6b}$$

$$\frac{\sigma_\phi}{k} = \left(\frac{a}{R}\right)^n \bullet \tilde{\sigma}_\phi\left(\frac{a}{R}, \frac{r}{R}, \theta, \nu\right), \tag{6c}$$

$$\frac{\tau_{r\theta}}{k} = \left(\frac{a}{R}\right)^n \bullet \tilde{\tau}_{r\theta}\left(\frac{a}{R}, \frac{r}{R}, \theta, \nu\right), \tag{6d}$$

in which the only independent parameter is now the relative contact radius a/R. Similarly the first principal stress field can be expressed as a function of a/R knowing the platen material:

$$\frac{\sigma_1}{k} = \left(\frac{a}{R}\right)^n \bullet \tilde{\sigma}_1\left(\frac{a}{R}, \frac{r}{R}, \theta, \nu\right). \tag{7}$$

Using Eq. (7), in Fig. 4 we plot the evolution of the k-normalized first principal stress, σ_1/k, versus the relative contact radius a/R for the sphere center (dashed line) and the surface equator (dotted line) together with the global maximum of the σ_1- field (solid line) for the two limiting values of n.

Over the course of a compression test, a/R increases steadily; thus, based on Figs. 2 and 4 and the discussion that precedes, the test can be divided into four successive stages or domains:

- Domain I: At the very beginning of a test, $(a/R) < 0.3$ and the highest tensile stress value within the particle is found near the sphere surface, either around the contact perimeter or along the compression axis just below the contact. Whether cracks will nucleate in those regions depends on the platen hardness relative to the particle strength.
- Domain II: Once a/R reaches ≈0.3, the location of the first principal stress global maximum shifts to the sphere center. Thereafter, magnitudes of the first principal stress in the center, and also along the equatorial belt, increase steadily as a/R increases. The former remains higher than the latter, the difference being as high as 40%. Therefore, if particle failure occurs in

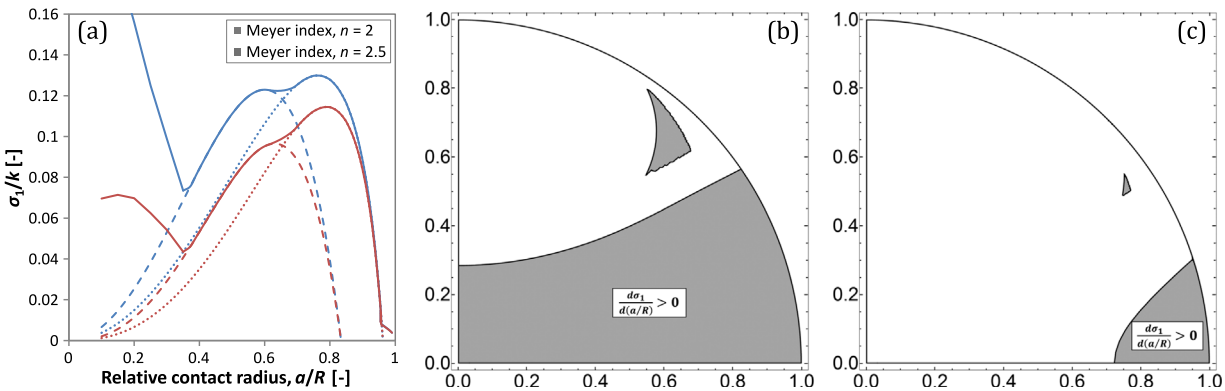

Fig. 4. (a) Evolution of the normalized first principal stress σ_1/k in the sphere center (dashed line) and along the surface equator (dotted line) versus the relative contact radius a/R, as obtained from Eq. (7). The global maximum of the field is shown with the solid line. The exponent of Meyer's law, n, used in calculations is 2 (blue) and 2.5 (red). In (b) and (c) grey areas show regions within the particle where the maximum tensile principal stress is increasing; (b): (a/R) =0.5; (c): (a/R) =0.7; for both, the platen Meyer index, n equals 2. Poisson's ratio of the sphere is ν=0.17.

this portion of the test, cracking can have initiated in either of the center of the sphere, or from its surface (Fig. 4b).

- Domain III: Then, at (a/R) ≈0.65, the stress at the center of the sphere starts decreasing while the peak stress location moves from the sphere center to its equator. From that moment on, stress levels in the central region of the particle have culminated while the tensile stress in the equatorial belt region keeps increasing. Therefore, if a particle has survived up to (a/R) =0.65 and then fails, its failure was caused by a flaw located near its equator, where tensile stress is still increasing (see Fig. 4c).
- Domain IV: Beyond (a/R) ≈0.78, regardless of the platen material, the stress starts decreasing everywhere within the particle: if it has not been broken yet it will (in principle) not do so in the test. So if loading is continued past this point, it will (in principle) only cause further embedding of the sphere into the platens - until the platens meet with the particle completely embedded and (a/R) =1.

This division of the test into four domains has several implications.

- The first is to show advantages inherent in the use of a platen material that is initially sufficiently soft and work hardens significantly: if n is near 2.5 then the peak stress value reached near the point of contact in early stages of the test (Domain I) remains lower than what can be attained later elsewhere within the sphere.
- The second is to show that if a sample fails within Domain III, then one *knows* that it failed at a flaw situated along its surface, near the equator. Here too, a platen with a high rate of work hardening is beneficial if surface defects are to be probed because the higher n is, the greater is the difference between the peak stress attained within the particle compared with the peak value attained later, near its surface, Fig. 4a.
- Finally, note that the optimal platen material must also be selected with an appropriate value of constant k in the Meyer law, Eq. (5), or in other words with an appropriate hardness, if it is to sample particle fracture stresses in their appropriate range. Since the Meyer hardness (in MPa) is roughly equal to k (Dieter, 1986), the platen material should be selected to have a hardness roughly equal to 8 times the expected particle fracture stress. Fig. 5 represents the relation between the required platen Meyer hardness for the expected particle strength assuming a platen material with n =2 and using Eq. (7) for three different particle Poisson ratio values. Note that with strong particles (failure stress on the order of few GPa), it may be difficult to find an appropriate platen material because hard materials tend to be brittle, which may lead to premature cracking of platens before reaching the required relative contact radius ≈0.7.

Values given above for the transitions between Domains I to IV were calculated for ν=0.17; for other values of ν, the test retains its qualitative features including the four domains but transitions occur at slightly different a/R values. In general, as ν increases, Domain III starts earlier and ends later in terms of a/R.

3. Materials and methods

Microscopic fused quartz particles were tested using the custom-built instrumented compression apparatus depicted in Fig. 6. The apparatus was designed to have a stiff load-train in order to minimize displacement of the load application platen upon failure of a tested particle, so as to minimize damage to the particle fracture surfaces. The device was therefore equipped with a high-stiffness miniature load cell XFTC300 (Measurement Specialities, Hampton, VA, United States) featuring a 10 N range and having a compliance near 0.1 μm/N (Fig. 6d). The relative force measurement error is typically below 1% in the range above 1 N. Upper platen movement during a compression test is controlled by a piezo actuator (Fig. 6c, article number P-843.60 by Physik Instrumente GmbH & Co., Karlsruhe, Germany), with a 90 μm displacement range. The compliance of the piezo actuator is also on

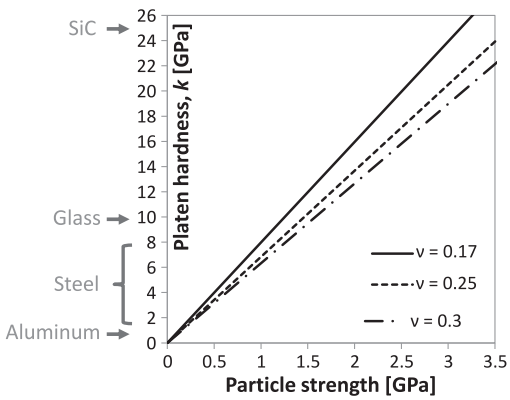

Fig. 5. Required platen Meyer hardness to test particles of given strength, assuming platen material with n =2 and relative contact radius at the moment of failure (a/R) =0.7. The three lines represent the relationship for three values of the particle Poisson ratio ν. Hardness values of the four materials indicated on the left are conversions to SI units of Brinell or Vickers hardness values from the literature (close although not exactly equal to Meyer hardness values).

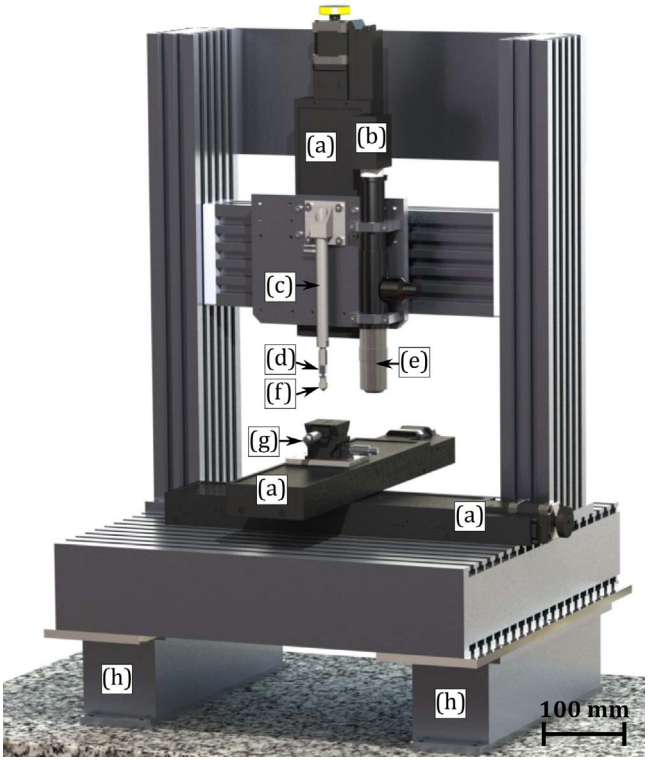

Fig. 6. Custom-built instrumented compression apparatus. (a) *x*-, *y*- and *z*-axis linear motion stages, (b) monochromatic camera, (c) piezo actuator, (d) high-stiffness load cell, (e) objective, (f) flat-end conical tip, (g) two-axis goniometric tilt stage, (h) active vibration-isolation system.

the order of 0.1 μm/N and its theoretical displacement precision is ≈10 nm. For general positioning, the apparatus features a system of three high-precision linear stages for *x*-, *y*- and *z*-axis motion (Fig. 6a). The measured overall load-train compliance of the apparatus is on the order of 1 μm/N. The testing apparatus is additionally equipped with an imaging system composed of a long working distance 20x objective (Fig. 6e) fitted to a 1.3 megapixel monochromatic camera (Fig. 6b). The whole set-up is mounted on an active vibration isolation table (Fig. 6h) in order to keep the noise amplitude in the load signal below 10 mN.

The load is applied at the top of individual particles, using interchangeable conical tips with a flat-end made of various materials that can be machined by conventional means (Fig. 6f), while a substrate in the form of a disk ca. 10 mm in diameter and 2 mm thick is used as the lower platen. This substrate is attached to a two-axis goniometric tilt stage (Newport Corp., Irwine, CA, United States) fixed onto the positioning stage (Fig. 6g), which was used in order to correct for any misalignments between the upper and lower platens. The two platens were thus kept plan-parallel within ~0.5°.

The conical tips and substrates were made of two different steels, namely AISI W1 and AISI 630. Steel AISI W1 was used in three different heat-treatment conditions resulting in four sets of platen materials covering the range of hardness between 450 and 950 HV; platen material details are presented in Table 1. The flat-end of the conical tip and the substrate were ground and polished using a diamond suspension prior to testing. Tip grinding and polishing was conducted using a fixture that kept the polished platen surface perpendicular to the axis of the tip, while protecting the edges with a small amount of epoxy resin that was subsequently removed by dissolution in acetone. The resulting diameter of the polished tip flat-end ready for testing particles was typically in the range of 200–300 μm. The Vickers Hardness of the tips and substrates was measured with a FM-300 (Future-tech Corp., Kawasaki, Japan) microhardness tester using a 0.5 or 0.3 kgf load on representative samples of the material. For all four platen materials, the spatial distribution of the hardness and elastic modulus values was analyzed using a series of 144 indents with contact area upon unloading

Table 1
The four platen materials.

Platen designation	Steel grade and condition	Nominal chemical composition (%)	Average measured Vickers Hardness
HV950	AISI W1, Q	1.05 C, 0.2 Si, 0.2 Mn, remainder Fe	930
HV750	AISI W1, QT		740
HV600	AISI W1, QT		600
HV450	AISI 630, AH	0.04 C, 0.25 Si, 0.4 Mn, 15.3 Cr, 4.5 Ni, 3.25 Cu, 0.3 Nb, remainder Fe	450

Note: letters after the steel grade designate the heat treatment condition: Q-quenched, QT-quenched and tempered, AH-age hardened.

on the order of 1 μm^2 using the TI 950 TriboIndenter® (Hysitron® Corporation, Minneapolis, MN, United States) nanoindentation apparatus equipped with a diamond Berkovich probe. In all cases the hardness and elastic modulus exhibited a unimodal distribution indicating homogeneous material behavior at contacts above 1 μm^2 in area, despite the known presence of fine carbides and precipitates in the AISI W1 and AISI 630 steels.

The compression tests were performed on amorphous spherical SiO_2 particles Denka FB-40S (Denka, Tokyo, Japan) of diameter typically between 20 and 60 μm. To observe the fractured particles after the test and prevent particle flyoff during fracture, a layer of isopropanol-based colloidal graphite paint (Pelco®, Redding, CA, United States) a few micrometers thick was applied using a brush along the substrate surface. The colloidal graphite layer keeps particles in place during the test and additionally works as a soft coating into which the particle sinks in the earliest phases of the test. The resulting soft belt of coating surrounds the particle along its equator, preventing particle fragments from flying off upon failure (as they otherwise will typically do). Particles of high sphericity were selected for testing, based on SEM images from which their diameter was measured to an estimated precision on the order of 2%. Prior to testing, individual particles were placed upon the graphite-coated substrate, and if necessary separated using a miBot™ (Imina Technologies SA, Lausanne, Switzerland) micromanipulator equipped with a tungsten needle.

The compression tests were performed using a constant upper platen displacement rate of 1 μm/s, lowered in a few instances to 0.5 μm/s. During a test, while the load gradually increases the steel platens deform plastically where they contact the particles. These gradually indent the upper and lower steel platen surfaces, increasing in turn the area of contact over which the load is applied to the particle. If the steel is hard enough to prevent the particle from completely sinking into the platens, then the tensile stress that develops within the particle and/or along its surface can cause failure from pre-existing flaws in regions of the particle that are not in direct contact with the platens, as shown above (Section 2).

The device was programmed to stop moving once an abrupt drop in load is detected. After each test, each individual indent left in the upper platen by the particles was observed using an optical microscope (Zeiss™ Axioplan 2, Oberkochen, Germany). Since the projected area of the indent does not change significantly upon unloading (Tabor, 1951), in data interpretation the measured indent radius is taken equal to the contact radius at the moment of failure, a. Relative error in a is estimated to be on the order of 5%. Each conical tip was used for up to five particle compression tests before it was changed, to ensure that all compression tests are performed using flat and polished regions of the tip several micrometers away from indents left by previous tests. Between two consecutive tests, the tip was cleaned of broken particle debris by pressing it against the graphite-coated substrate with a force of ~5 N; this traps debris left along the flat steel tip surface within the graphite. All tests were carried out at room temperature in air (relative humidity between ~20 and ~50%).

The micron-sized graphite particles present in the colloidal graphite paint, tiny debris particles that might be present on the surface of the tested fused quartz particles, fine carbide particles or other precipitates present in the steel platens or even a possible dislocation pile up near the platen-particle contact interface may locally concentrate stress along the platen/particle interface during the test, potentially causing a second, alternative failure site. If one takes a worst-case scenario and assumes that all such local contact perturbations (graphite particles, debris, precipitates, etc.) act as minute elastic spherical particles that indent the surface of the compressed sphere, by performing a simple analysis using Hertzian elastic contact theory (Supplementary material, Section 2), one finds that the only place where such a local inhomogeneity may cause, locally, significant tensile stress in the surface of the compressed particle is when the inhomogeneity is along the platen-particle contact perimeter. Having the inhomogeneity situated precisely there is of course unlikely. Moreover, the fact that the volume of the tested particle exposed to the local tensile stress concentration created by such an extraneous stress-concentrator is significantly smaller than the volume of the particle that is exposed to elevated tensile stress around the equatorial belt reduces further the probability of failure from such stress concentration sites along the contact perimeter. In our analysis we thus do not consider the possibility that failure of the compressed particle is initiated by local stress concentrators such as those enumerated above.

4. Results

Eighty-five (85) spherical fused quartz particles were tested in compression; of these, twenty-five (25) particles were tested for each platen having hardness HV450, HV600 and HV750, while 10 particles were tested using the platen of hardness HV950. Fig. 7 shows a typical force-displacement curve recorded during a compression test, along with pictures of the particle before and after the test, and also of the indent left in the steel platen after the test (giving the contact radius at the moment of failure).

At the start of each test, the upper platen travels at constant displacement rate until it touches the particle. The particle then starts to sink into the soft ≈10 μm thick colloidal graphite layer; this phase is exhibited by the first shallow non-linear force displacement response. Once the particle touches the underlying steel platen the force-displacement curve steepens significantly. The force then increases up to the moment of failure, reaching its critical (particle fracture) value typically indicated by a sharp drop in load; at this moment the test is automatically terminated. The full set of experimental data is given in Appendix B, Table B1.

Fig. 8 gives the measured values of the critical force divided by the particle cross-sectional area, $F_{max}/\pi R^2$ versus the relative contact radius a/R at particle failure for the four different platen materials. As seen, after normalization of $F_{max}/\pi R^2$ with the Vicker's hardness HV (in SI units) of the relevant platen, all the data collapse onto a single curve, as predicted by Meyer's law, Eq. (5). Fitting the master curve with a power law, we find n =2.2 and $\tilde{k} = k/HV$=1.2. Note that exponent n is related to the strain-hardening coefficient of the platen material; since each of the platens is of hardened steel, that all four platens have a similar strain-hardening exponent is reasonable.

Fig. 9 gives values of the first principal stress within each particle at the moment of failure, as calculated using the HO-SH

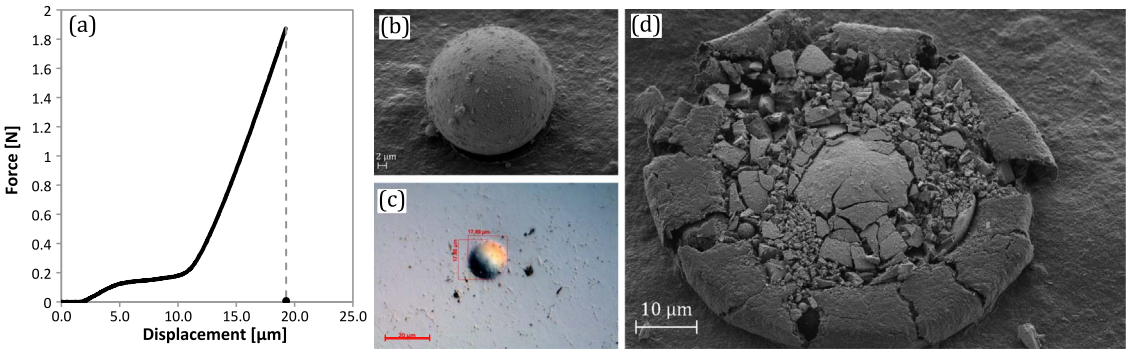

Fig. 7. Typical uniaxial compression test of a fused quartz particle: (a) force-displacement curve. Initial non-linear part of the response represents the embedding of the particle in the soft colloidal graphite layer. Contact between the particle and the steel platen is marked by a significant increase of the response slope; (b) and (d) scanning electron microscopy images of the particle before and after the test; (c) optical image of the upper platen surface showing the indent left by the particle after the test.

analysis using measured values of (F_{max}, a/R). Fig. 9a gives the calculated first principal stress in the center of the sphere, σ_{1c}, while Fig. 9b plots the first principal stress along the equatorial line, σ_{1s} at that moment. The dashed lines in Fig. 9 trace the predictions for the evolution of the first principal stresses, σ_{1c} and σ_{1s}, versus a/R, calculated using the HO-SH solution coupled with the particular platen Meyer law obtained in Fig. 8 according to Eq. (7). As can be seen, the curves fit the data, showing that the two calculations are mutually consistent.

Dashed vertical lines in Fig. 9 indicate the four failure domains of internal particle stress distribution that were discussed in the Theory section. Domain I, where $(a/R) \leq 0.3$, is absent as no data lie within this region: particle failure hence did not initiate from the near-contact regions in the present tests. Of the 85 tests, we find that 23 failure events occurred with $(a/R) \pm \Delta(a/R)$ situated within the range from 0.65 to 0.78, i.e., in Domain III within experimental error. According to the analysis presented above, we know that failure of those 23 particles was initiated from the particle surface, along the equatorial belt.

Let us ignore for now other particles, and consider only those 23 particles. In Domain III, each platen probes particle strength values situated within a specific range determined by the following bounds:

- the surface stress σ_{1s} value at the moment when the central stress σ_{1c} starts to decrease, i.e. when $(a/R) \approx 0.65$ for fused quartz (ν=0.17);
- the highest value of stress σ_{1s} attainable by each platen, which is reached for fused quartz (ν=0.17) when $(a/R) \approx 0.78$. In Domain III particle strength values must therefore fall in the range $550 \leq \sigma_{1s} \leq 650$ MPa for platens with HV450, $700 \leq \sigma_{1s} \leq 900$ MPa for platens with HV600, $900 \leq \sigma_{1s} \leq 1100$ MPa for platens with HV750 and $1100 \leq \sigma_{1s} \leq 1300$ for the hardest platen, of HV950.

Of the 85 tested particles, 27 other particles entered Domain IV, where $(a/R) > 0.78$. Of these, 18 particles that were tested using the softest HV450 platen did not crack at all: those were fully embedded and the platens contacted; in graphs in Fig. 9 these are shown with the symbol to the far right. More surprisingly, 9 other particles that entered Domain IV actually failed, even though according to theory σ_1 was decreasing everywhere within the particle. A likely cause of these nine failure events is delayed fracture,

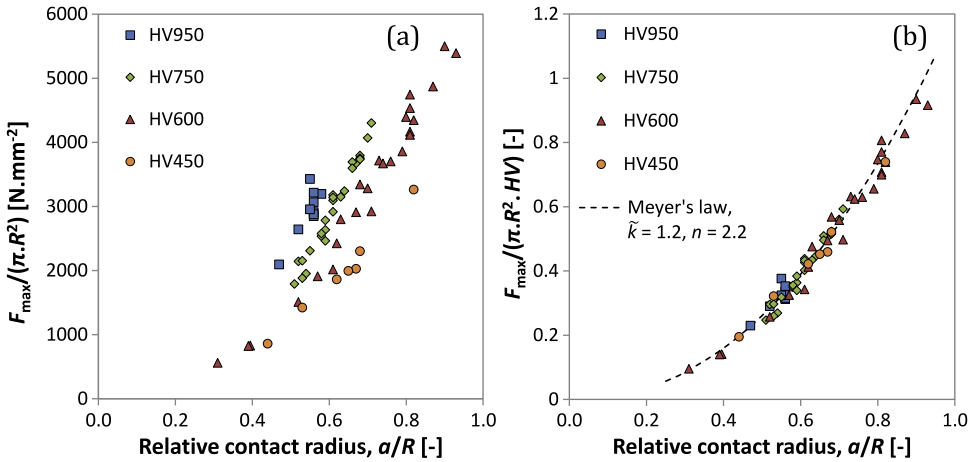

Fig. 8. (a) Experimentally measured values of the critical force divided by the particle cross-sectional area, $F_{max}/\pi R^2$, versus the relative contact radius a/R. (b) The data align on a master curve when normalized by the Vicker's hardness HV in SI units. The dashed line represents the least squares fit of Meyer's law giving $\tilde{k} = k/HV$=1.2 and n =2.2.

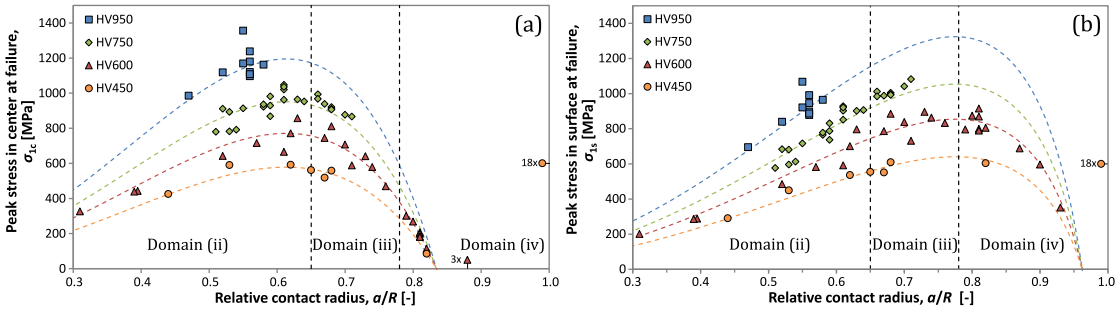

Fig. 9. First principal stress versus the relative contact radius a/R: (a) in the center of the compressed particle,σ_{1c} and (b) along the surface equator, σ_{1s}. Symbols represent calculated stress values using the HO-SH analysis, Eq. (4), based on measurements of the critical load at failure F_{max} and corresponding relative contact radius a/R. Dashed lines give predictions for σ_{1c} and σ_{1s} based on the HO-SH solution and Meyer's law (Fig. 8 and Eq. (7)). Symbol shape and color indicate the platens used: HV450 (circle, orange), HV600 (triangle, red), HV750 (diamond, green) and HV950 (square, blue). Vertical lines separate different failure domains, as discussed in the Theory section. For color see on-line article version.

known to operate when fused quartz material is tested in (humid) ambient air (see Section 5.3). To test this hypothesis, one particle was compressed using HV600 platens up to (a/R) ≈0.87, whereupon platen movement was paused, thereby leaving the particle under static compressive loading with the tensile stress peaking along the surface equatorial belt at a value around 600 MPa. This test is summarized in Appendix C; after several tens of seconds, the particle failed with an abrupt drop in load, thus giving indirect proof that slow crack growth is operative in the tested particle material.

The colloidal graphite paste proved effective in retaining the broken particles pieces after fracture, see Figs. 7d and 10. Most failed particles show extensive shattering (Figs. 7d and 10a); with such fragmented particles it was generally impossible to determine the cause of failure by means of fractography. In some cases the colloidal graphite paste could not contain all particle pieces after shattering, suggesting the presence, within the particles, of regions under substantial compressive stress (Kelly and Spottiswood, 1990). Particles that broke at lower tensile stress values showed a much smaller number of fragments.

In some cases, when shattered particle fragments were big enough, we could observe a few fractographic details related to the cracking process. An example from a particle that broke in Domain II after testing with the HV950 platen is shown in Fig. 10a. This fragment represents one-half of a central column extending roughly from the particle center to the bottom platen surface. By detailed observation of the fragment, river markings can be identified, which indicate the local direction of crack growth (Hull, 1999). For this example, the river pattern indicates that the prevailing crack growth direction along the column surface was from the particle center towards the area of contact with the platen.

Two other examples of particles that failed at relatively low stress levels are presented in Fig. 10b and c. Both particles were tested with the HV450 platens and their fragmentation was limited. In Fig. 10b, the particle failed in Domain III, which is consistent

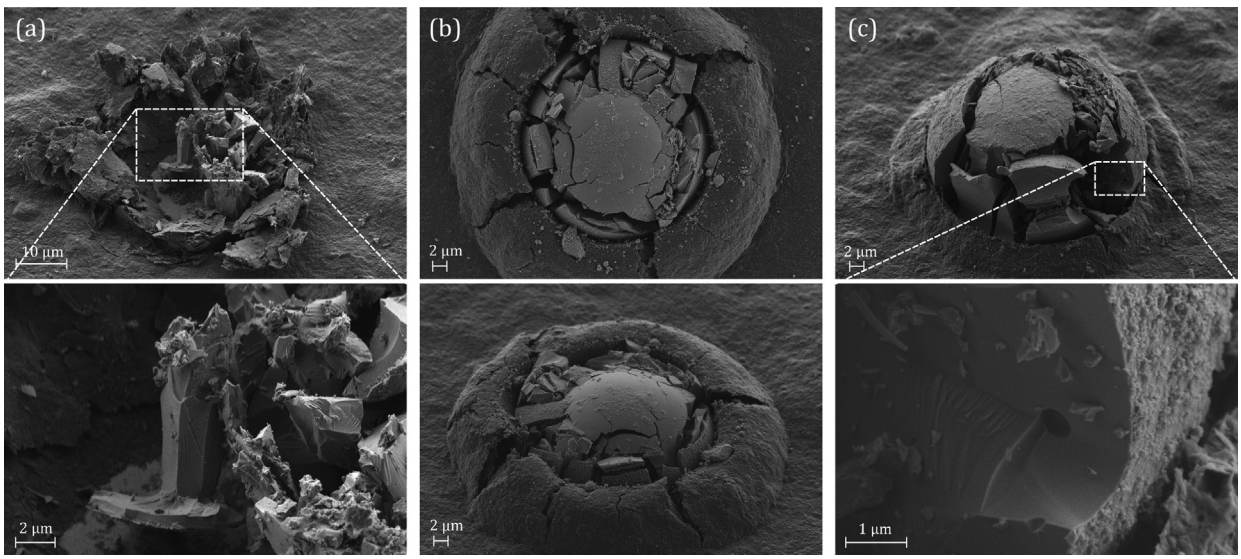

Fig. 10. SEM images of particles after uniaxial compression testing. (a) Particle that failed at (a/R) < 0.65 (in Domain II), shattered into many pieces but leaving a central column roughly extending from the lower surface to the particle center, along which river markings suggest crack growth from the particle center to a point of load application. (b) and (c) show two particles that failed at relatively mild surface peak stress values, namely 610 and 450 MPa, respectively. The particle in (b) failed at (a/R) > 0.65 (Domain III): several meridian cracks are visible, consistent with the predicted stress distribution at that moment. The particle in (c) failed at (a/R) < 0.65 (Domain II); a subsurface pore can be observed along the path of one meridian crack, with river markings suggesting crack growth away from the pore.

with the observed failure pattern consisting of several meridian cracks, with the region of contact with the metallic platens essentially intact, unlike what is seen when hard platens are used (Chaudhri, 2004; Majzoub and Chaudhri, 2000).

The particle in Fig. 10c failed with (a/R) =0.53, i.e., well within Domain II, however, a subsurface pore can be found along the fracture surface of one meridian crack near the particle equator. The fractographic pattern with river markings present near the pore is consistent with it being the origin of failure (although this evidence is not conclusive since not all fragments could be examined).

5. Discussion

5.1. Survival analysis for data points known to be measures of the surface strength

To interpret the present strength data, we adopt a point of view similar to that of Shipway and Hutchings (Shipway and Hutchings, 1993b), namely that compressed particles will generally break either near their center, or near their equator, meaning from defects situated either in the midst or along the surface of the particles. For simplicity, we ignore the influence of particle size. To simplify writing, in what follows Domain III will be used to designate those particles for which $[\frac{a}{R}+\Delta(\frac{a}{R})]>0.65$ and $[\frac{a}{R}-\Delta(\frac{a}{R})]<0.78$, where $\Delta(\frac{a}{R})$ is the estimated absolute uncertainty in relative contact radius measurement. The rest belongs either to Domain II ($[\frac{a}{R}+\Delta(\frac{a}{R})]<0.65$at fracture) or Domain IV ($[\frac{a}{R}-\Delta(\frac{a}{R})]>0.78$ during the test). Terms *surface stress* and *center stress* will be used for the instantaneous local peak value of the tensile first principal stress along the equatorial line, σ_{1s}, and particle center, σ_{1c}, respectively.

The strength of the tested particles is statistically distributed: we thus do not aim to assess an average particle strength, but rather aim to measure the particle statistical strength distribution. To this end, we rely on the extensive statistical analysis work that has been developed over the past few decades to analyze banks of data of similar nature, commonly found in medical studies and pertaining to survival probabilities; Ref. (Klein and Moeschberger, 2003) gives a clear, user-friendly, overview.

If we replace time, commonly used in Survival analysis, with stress, and acknowledge that we have here two competing causes for failure (center failure and surface failure), we have here a survival analysis problem with two somewhat peculiar characteristics, namely:

(i) whereas time in classical lifetime analysis is a common parameter used to track all causes of mortality, here failure at the center or at the surface of the particles is caused by one of two (local) stress values that differ at each instant; and
(ii) because those two local stresses do not always increase together (Section 2), the present data have the peculiar feature that there is a window of surface stress values within which one knows the cause for failure: all strength data that occurred in Domain III are *known* to relate to meridian cracking initiated at, or very near, the equator surface.

Furthermore, by varying the hardness of the platens, one varies the range of surface stresses imposed on a particle. Therein lies one of the most attractive features of what we call here the meridian test.

With these specificities noted, statistical methods of survival analysis can be transposed to the present situation. We assume that flaw distributions within the center and along the surface of the particles are independent; *a priori* this should be reasonable given their different nature (pores versus surface cracks). Since surface flaws are known to be at the origin of failure in several of the present particles (all those that broke in Domain III; see also Fig. 10c), we focus on this cause for failure first, to then later turn our attention to the possibility of failure starting in the center: as will be seen its importance for particles tested here is comparatively minor, as could be anticipated for glass spheres. Two approaches can be used, namely non-parametric analysis (which assumes nothing of the flaw size distribution) or a parametric approach, which assumes that the particle surface strength is Weibull distributed. We present both in turn; Appendix D shows a comparative illustration of the two approaches on a hypothetical set of Weibull distributed data with features similar to those in the present experiments.

5.1.1. Non-parametric survival analysis

Here, we assume nothing of the flaw or strength distributions along the center or surfaces of the particles. To estimate the failure probability at a given stress level we use the Kaplan-Meier product limit estimator (Kaplan and Meier, 1958; Klein and Moeschberger, 2003) adapted for left-truncation and right-censoring of the data.

Particle failure within Domain III is known to have originated from the particle surface; hence in an analysis of the surface strength distribution of particles, such events provide hard, unambiguous data. Additionally, particles from Domain IV survived the maximum attainable stress that can be imposed by the given platen material (regardless of whether a few failed later on). In other words we know a lower bound of their surface strength; in survival analysis, events of Domain IV are named right-censored data of Type I (Klein and Moeschberger, 2003). Those events include 8 particles tested using HV600 platen (which failed in Domain IV, most probably due to slow crack growth as explained above) - and 19 particles tested using the HV450 platen, one of which also failed in Domain IV, again likely due to slow crack growth, while the remaining 18 sank into the platens without breaking. The censoring level of surface stress values are 900 MPa for HV600 and 650 MPa for HV450 platens, respectively.

Those data from Domains III and IV trace only a portion of the strength distribution, since strength is bound from below by the surface stress value at which Domain III starts for a given platen material. In the language of survival analysis, all events, being either failure or right-censored, from Domains III and IV, are left-truncated for values of (surface) strength below the onset of Domain III: the left-truncation surface stress values were approximately 900 MPa for HV750, 700 MPa for HV600 and 550 MPa for HV450 platens, respectively.

Table 2
Results used for surface strength survival analysis.

Platen	Measured failure/ censoring peak surface stress [MPa]	Censoring indicator[a]	Left-truncated at [MPa]	Platen	Measured failure/ censoring peak surface stress [MPa]	Censoring indicator[a]	Left-truncated at [MPa]
HV750	990	0	900	HV450	650	1	550
	1000	0	900		650	1	550
	1080	0	900		550	0	550
	1040	0	900		650	1	550
	1000	0	900		650	1	550
	990	0	900		650	1	550
	910	0	900		650	1	550
	900	0	900		650	1	550
	1010	0	900		650	1	550
	980	0	900		650	1	550
HV600	900	1	700		650	1	550
	900	1	700		650	1	550
	900	0	700		650	1	550
	890	0	700		610	0	550
	870	0	700		650	1	550
	860	0	700		650	1	550
	800	0	700		650	1	550
	840	0	700		650	1	550
	790	0	700		650	1	550
	900	1	700		650	1	550
	900	1	700		550	0	550
	900	1	700		650	1	550
	830	0	700				
	900	1	700				
	900	1	700				
	900	1	700				
	800	0	700				
	730	0	700				

[a] when 0, the surface stress represents the surface strength measurement, otherwise value 1 indicates righ-censoring and the value in the surface stress column represents lower-bound of the surface strength.

Consider now the ensemble of data from Domains III and IV: there are D distinct known surface failure stresses $\sigma_{1s}^1 < \sigma_{1s}^2 < \ldots < \sigma_{1s}^D$ for events in Domain III, and C right-censored events of Domain IV. Note that if two particles fail at the same surface stress, σ_{1s}, this translates here into one value of σ_{1s}^i ; therefore D is a number lower or equal to the number of particles that failed within Domain III.

One can thus analyze the data using the non-parametric product-limit estimator defined as follows:

$$P_i(\sigma_{1s}) = \begin{cases} 1 & \text{if } \sigma_{1s} < \sigma_{1s}^1 \\ \prod_{j=1}^{i}\left(1-\frac{d_j}{Y_j}\right) & \text{if } \sigma_{1s} \geq \sigma_{1s}^1 \end{cases} \tag{8}$$

where index $i \in \{1, \ldots, D\}$, P_i is the probability of survival at stress σ_{1s}^i, d_j is the number of particles that failed at the stress equal to the σ_{1s}^j and Y_j is the number of particles that have survived at least stress σ_{1s}^j and at the same time have a left-truncation stress T lower or equal to the failure stress σ_{1s}^j, including censored particles; this quantity represents the number of particles *at risk*. Data used for non-parametric survival analysis of the surface strength are given in Table 2.

5.1.2. Parametric survival analysis

Alternatively, we can assume that the surface strength of the fused quartz particles follows a given distribution and estimate parameters of that distribution. Here, we use the two-parameter Weibull distribution with shape parameter m and scale parameter σ_0. Using similar left-truncation and right-censoring of the data, we estimate those parameters by maximizing the log-likelihood function given by (Balakrishnan and Mitra, 2012)

$$\log L = \sum_{j=1}^{N} \{-(1-\delta_j)\bullet\log(1/m)+\delta_j\bullet m(\log\sigma_{1s}^j - \log\sigma_0) - \exp[m(\log\sigma_{1s}^j - \log\sigma_0)]\} + \sum_{j=1}^{N} \nu_j \exp[m(\log T_j - \log\sigma_0)], \tag{9}$$

where, σ_{1s}^j is an observed event (a failure or a censored surface stress value), δ_j is the censoring indicator equal either to δ_j =1 if the j-th observation is censored or 0 if the data point corresponds to an observed failure event, T_j is the corresponding left-truncation peak surface stress value, ν_j is the truncation indicator (in our case always with value 1) and N is the total number of particles in Domains III and IV.

Statistical analysis of the data was conducted using the computational program *Mathematica* v. 10.1 (Wolfram Research Inc.,

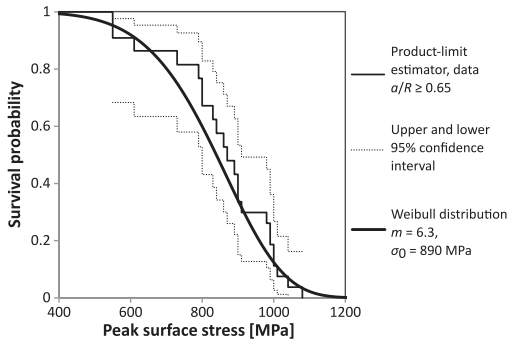

Fig. 11. Estimated particle surface strength distribution computed using only data for which (a/R) ≥0.65 (Domains III and IV), using left-truncation and right-censoring according to the non-parametric Product-limit estimator, plotted together with 95% point-wise confidence intervals, or alternatively assuming Weibull statistics coupled with a maximum likelihood estimation of parameters.

Champaign, Illinois) with built-in functions *SurvivalModelFit* for the Product-limit estimator and *EstimatedDistribution* for the Maximum likelihood estimation using data from Table 2.

The result is shown in Fig. 11; as seen the two estimations come close to one another. The parametric estimation gives m =6.3 and σ_0 =890 MPa.

5.2. Interpreting data for competing center and surface failure

Four particles failed at low stress values, namely σ_1 ~300–400 MPa in the center, and displayed along their fracture surface large and clearly apparent internal pores. Exempting those four particles (which represent roughly 5% of all tested particles) from further consideration, given how different their fracture stress and failure mode are from what was found with all other particles, we now examine particles that failed in Domain II. With those particles, we do not know whether fracture was initiated from a flaw along their surface near its equator (the only scenario in Domain III) or from a volumetric flaw situated near their center. Knowing the above estimation of the surface strength derived from consideration of data in Domains III and IV, however, we can test whether data in Domain II indicate the presence of another cause for failure (necessarily flaws in the particle center) or whether, on the contrary, those data are consistent with surface flaws being the dominant determinant of strength for the particles at hand.

To this end, we repeat the non-parametric product-limit analysis as well as the maximum likelihood estimation of Weibull strength distribution parameters using the surface peak stress values, σ_{1s} at the moment of failure, looking now only at data points in Domain II. Here, each platen measures the surface stress only up to a certain value that is again given by the platen material, which equals the values used for the left-truncation in the precedent analysis. In survival analysis terms, we now right-truncate the data of Domain II by the value of σ_{1s} at the onset of Domain III. In practice, due to scatter in the data along the theoretical surface stress vs. (a/R) relation (Fig. 9b), the highest observed value of σ_{1s} for $(a/R) < 0.65$ for each platen dataset was taken as the right-truncation value. Left-truncation is now irrelevant (we observe failure events starting at σ_{1s} =0 MPa). Additionally, we exclude from the analysis the four low-stress particle failure events for which a big internal pore was observed (see Appendix C, Fig. C2). The construction of the product-limit estimator is somewhat different than in the case of left-truncated/right-censored data (Klein and Moeschberger, 2003); here we again use *SurvivalModelFit* function of the computational program *Mathematica* v. 10.1.

The survival analysis of data from Domain II in terms of the surface stress is presented in Fig. 12 along with the analysis derived from the data set in Domains III and IV discussed in Section 5.1. As seen, the two essentially coincide. There is thus, in the present

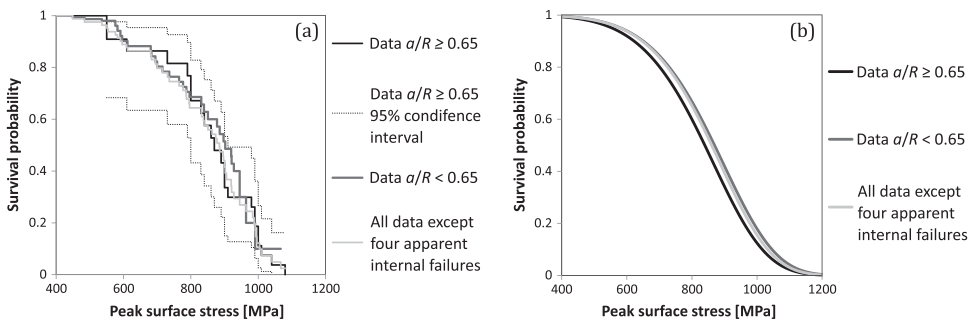

Fig. 12. (a) Product-limit estimation of particle surface strength for particle populations from (black) Domains III and IV (left-truncated/right-censored data), together with (black dotted) corresponding 95% point-wise confidence intervals, (dark-grey) data from Domain II (right-truncated data), and (light-grey) ensemble of all data points (right-censored) except for four particles containing evident large pores, which failed at low stress. (b) The same three data sets with their maximum likelihood estimation of two-parameter Weibull distribution parameters: (black) m =6.3 and σ_0=890MPa, (dark-grey) m =6.5 and σ_0=920 MPa, (light-grey) m =6.6 and σ_0=910 MPa.

data, insufficient evidence to reject the hypothesis that all except four particles tested here failed by cracking from a flaw situated along their surface.

If we now lump together all data (from Domains II, III and IV) excepting still the four particles with big internal pores, we have 54 surface failure events and 27 right-censored data in the form of particles that entered Domain IV. Using the built-in function *EstimatedDistribution* in the *Mathematica* computation software, the maximum likelihood estimation of the two-parameter Weibull distribution particle strength distribution become m =6.6 and σ_0=910MPa; the change in these values is by only 6% and 2% compared with the initial estimate based on the subset of data from Domains III and IV alone. Since data are consistent with surface failure being the dominant failure mode in the present particles, this can be viewed as a reliable estimator of their surface strength distribution.

The characteristic strength value σ_0=910MPa translates to a critical half penny-shape surface crack situated along the equator, $c = 370$ nm if we use the linear-elastic fracture mechanics expression, $c = \left(\frac{K_{IC}}{Y \bullet \sigma_0}\right)^2$ where the fracture toughness, K_{IC} of fused quartz is 0.65 MPa m$^{1/2}$ (Žagar et al., 2016, 2015a) and the geometric factor, Y for a half penny-shape crack of negligible size with respect to the size of a particle is $0.66 \bullet \sqrt{\pi}$. For comparison, the pore observed near the surface on one of the tested particles in Fig. 10c has a diameter of roughly 500 nm, which is thus consistent with the calculated Weibull strength parameter value.

Surface flaws as well as humidity are well known to govern the strength of fused quartz (Armstrong et al., 2000; Proctor et al., 1967). Unless a protective coating is applied, surface flaws will generally be caused by surface abrasion during storage and handling of the powder. Comparing particles tested here with other data for fused quartz one finds that the present particles are, with their strength on the order of 1000 MPa, strong compared to macroscopic fused quartz or silica glass particles, which typically fail at 200 MPa or lower (Huang et al., 2014; Shipway and Hutchings, 1993b). Yet the particles are far less strong than what can in principle be achieved: fibers of fused quartz tested in vacuo at −196 °C approach the theoretical strength value of 15 GPa, while the strength in air at room temperature of these almost defect-free fibers was in the range of 4–7 GPa with evident dependence on the stress rate (Proctor et al., 1967). The industrial-scale manufacturing of spherical fused quartz particles much stronger than those tested here should, thus, be possible.

5.3. Effect of slow-crack-growth

Particle strength data measured above were obtained in ambient air, in which it is well known that fused quartz is susceptible to delayed cracking caused by slow-crack-growth (SCG) (Armstrong et al., 2000; Salem, 2013; Suratwala and Steele, 2003; Wiederhorn and Bolz, 1970; Žagar et al., 2015b). As indicated above, the observation that a few particles failed within Domain IV, coupled with the steady load test reported in Appendix C, are strong indicators that SCG was active in the present particles. We therefore estimate the influence of the phenomenon on the strength of the present particles, in an attempt to derive what their strength distribution might be in the absence of the phenomenon, e.g., in an inert environment, or when they are embedded within a composite material having a matrix impervious to water.

The kinetics of SCG are often modeled assuming the power-law characteristic of the first stage of SCG (i.e., by assuming that crack tip velocity saturation has not been reached) given by

$$\frac{dc}{dt} = AK_I^r \tag{10}$$

where c represents the instantaneous size of a sharp crack, t is time, K_I is the Mode I stress intensity factor and A and r are constants that depend on the material and environment. Assuming for simplicity that loading is conducted with a constant stress rate, $\dot{\sigma}$, then the stress at failure in the presence of SCG of a solid containing an initial flaw of size c_i, as derived by (Evans and Johnson, 1975), is

$$\sigma_{SCG} = \left(\frac{2(r+1)\dot{\sigma}}{(r-2)AY^r c_i^{\frac{r-2}{2}}}\right)^{\frac{1}{r+1}}, \tag{11}$$

where Y is the geometric factor giving the stress intensity factor as $K_I = Y\sigma\sqrt{a}$. In the absence of SCG, the same solid containing the same initial flaw of length c_i would fail at stress

$$\sigma_t = \frac{K_{IC}}{Y\sqrt{c_i}}, \tag{12}$$

where K_{IC} is the fracture toughness. SCG parameters for fused quartz at room temperature and ~70% relative humidity are given in the literature as r =34 and $A = 8\times10^6$ (Suratwala and Steele, 2003). With $Y = 0.66 \bullet \sqrt{\pi}$ for a half-penny crack of size negligible compared to that of the tested body, a fracture toughness 0.65 MPa m$^{1/2}$ (Mueller et al., 2015; Žagar et al., 2016) and c_i in the range of 0.1 – 1 μm, with $\dot{\sigma}$ =1 GPa/s, SCG will reduce the strength to between 61% and 68% of the inert strength σ_t. In order to measure at least 95% of the inert strength, $\dot{\sigma}$ would have to be far above what can be achieved by conventional means. The effects of SCG must therefore be considered in interpreting the present data.

The majority of tests in the present study used an upper platen displacement rate that was dh/dt=1μm/s; in a few cases the rate was dh/dt=0. 5μm/s. Considering perfectly spherical particles, the relative contact radius as a function of time is given by

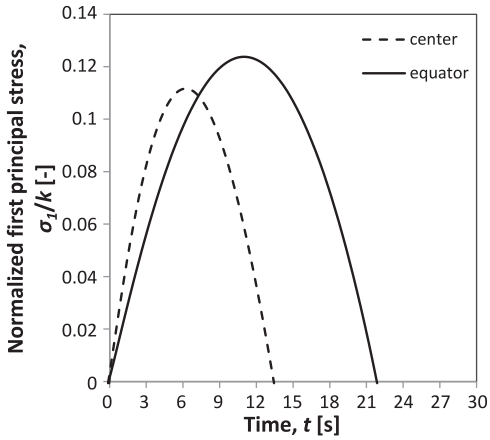

Fig. 13. Evolution of the normalized first principal stress for a fused quartz particle with 15 μm radius loaded with upper platen displacement rate 1 μm/s and Mayer's law index of the platen n =2.2.

$$\frac{a}{R} = \sqrt{\frac{\frac{dh}{dt}\bullet t}{R} - \frac{\left(\frac{dh}{dt}\bullet t\right)^2}{4R^2}}, \tag{13}$$

Combining Eqs. (13) and (7) and taking a typical value for R =15 μm, with a Meyer's law index n =2.2 as observed for the platens of this work and dh/dt=1μm/s, one obtains the evolution of the adimensional stress $\frac{\sigma_1}{k}$ as a function of time t presented in Fig. 13. As can be seen from the figure, in a typical test of this work it takes ~7 s from the beginning of the test to reach Domain III. Thereafter, the surface stress in Domain III still increases for about ~3.5 s, and once in Domain IV it remains at a relatively high level for another ~3.5 s. Thus, the total time, on the order of couple of seconds, that a tested particle spends at high surface stress in Domains III and IV, might be sufficient for a surface flaw to grow due to SCG to reach a critical size, and thereby cause a particle to fail when it would not in an inert environment. This explains the occurrence of several failure events past the point of maximum surface stress.

With SCG active, the measured strength depends on the stress rate. Inserting Eq. (12) into Eq. (11), one obtains the relation linking the inert strength σ_t and the measured strength, σ_{SCG}, as reduced by SCG

$$\sigma_t = \left(\sigma_{SCG} \Big/ \left[\frac{2(r+1)}{(r-2)}\frac{\dot{\sigma}}{A\bullet Y^2 K_{IC}^{r-2}}\right]^{\frac{1}{r+1}}\right)^{\frac{r+1}{r-2}}. \tag{14}$$

where σ_{SCG} now represents the measured surface strength σ_{1s} in this work in Domain III and a lower bound of the strength for particles from Domain IV. We assume surface half-penny shape flaws of size well below R, SCG kinetics according to Eq. (10), and (although this is not true here) loading under a constant stress rate. Specifically, we take $\dot{\sigma}$ equal to the secant stress rate, that is, we divide σ_{1s} at the moment of failure by the time under load up to failure. Typical values of the secant stress rate were on the order of 100 MPa s^{-1}, with the range of values between 20 and 130 MPa s^{-1}. The estimated intrinsic surface strength, σ_t from Eq. (14) then represents the surface strength that the particle would display in the absence of SCG, as given by Eq. (12). For particles that entered Domain IV (for these we only know a lower bound of their surface strength), we take σ_{SCG} equal to the maximum attainable peak surface stress during the test for the relevant platen. Eq. (14) then gives a lower bound for σ_t: in other words, these again form right-censored data.

Correcting the strength values of the data from Domains III and IV for the effects of SCG gives again a left-truncated and right-censored dataset on which we can use the Survival analysis methods as exposed earlier. For simplicity the left truncation level was taken as the lowest observed SCG corrected surface strength, σ_t for each platen dataset (HV750, HV600, HV450). Fig. 14 gives the resulting estimated particle strength distribution: as seen, SCG causes the high-strength part of the distribution to shift to significantly higher strength values: it is thus likely these particles would be far stronger in an inert humidity-free environment, notably when used as a reinforcement in a composite with a matrix impervious to moisture. This said, even after correction for the effects of SCG, the measured strength distribution remains far below what is achieved in glass fibers: particles such as these should be sized and handled with greater care if they are to be used as a composite reinforcement.

6. Conclusion

Building on the approach of Shipway and Hutchings, we show how uniaxial particle compression testing can be improved if one uses a pair of elasto-plastic platens of tailored hardness, selected to be sufficiently soft relative to the particle such that measured strength values do not reflect the influence of Hertzian contact stress concentration, while being sufficiently hard to crack the particles in the appropriate range of indent to particle radius ratio values. The different trajectories of peak tensile stress near the center, and along the surface of the particles, are such that the distribution of central and surface strengths can be separately

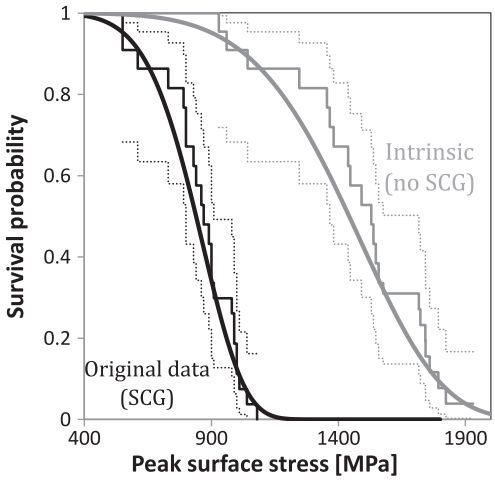

Fig. 14. Comparison of the peak surface strength distribution of the (black) original data (influenced by SCG) and (grey) same after correction for the effect of SCG. Smooth solid curves represent the estimated Weibull distributions using a maximum likelihood method; corresponding parameters are m =6.3, σ_0=890 MPa and m =5.6, σ_0=1540 MPa for the original and SCG corrected data, respectively. The solid stepped curves represent the Product-limit estimator, together with corresponding dotted curves representing 95% point-wise confidence intervals of the Product-limit estimator.

assessed from test data conducted using appropriately chosen platen materials and the methods of survival probability analysis.

The approach is demonstrated using commercially available spherical microscopic fused quartz particles 30 μm in average diameter (Denka FB-40S produced by Denka, Tokyo, Japan). Tested in air with a loading rate on the order of 100 MPa s^{-1} the particles show strengths between 500 MPa and 1100 MPa with a characteristic strength value near 900 MPa. Roughly 5% of the particles fail at far lower strength values, in the range ~300–400 MPa, that are caused by the presence of large internal pores. The remaining 95% of the particles have surface-flaw limited strength distributions that can be described using two-parameter Weibull distributions of parameter values m =6.6, σ_0 =910 MPa for the particles tested in air, corresponding to estimated values of m =5.6, σ_0 =1540 MPa if the particles are protected from humidity.

Acknowledgement

This research was funded by the European Research Council under the European Union's Seventh Framework Programme (FP/2007–2013) / ERC Advanced Grant Agreement No. 291085. Authors acknowledge the initial exploratory experiments performed by Dennis Lang and Adrien Mazuryk conducted in the context of this project in their semester and summer projects, respectively.

Appendix. A

Hiramatsu and Oka published a solution for the stress tensor components within particles compressed as in Fig. 1b (Hiramatsu and Oka, 1966). The original paper contained some typos and errors, which were corrected in later publications: corrected expressions for $\tilde{\sigma}_\theta$, $\tilde{\sigma}_\phi$, $\tilde{\tau}_{r\theta}$ were published in (Oka and Majima, 1970) and the expression for $\tilde{\sigma}_r$ can be found in (Hiramatsu and Oka, 1967)). Corrected expressions used here are (the original equations from (Oka and Majima, 1970) contained few typos):

$$\sigma_\theta=-\frac{1}{2}\left[1+\sum_{i=1}^{\infty}\left(\frac{-(4i+1)(i-1)+(4i+1)^2\nu}{2i(4i^2+2i+1)+2i(4i+1)\nu}\left(\frac{r}{R}\right)^{2i}+\frac{(4i+1)(4i^2+4n-1)+2(4i+1)\nu}{2(4i^2-1)(4i^2+2i+1)+2(4i+1)(4i^2-1)\nu}\left(\frac{r}{R}\right)^{2i-2}\right)\bullet(1+\cos\alpha)\bullet P'_{2i}(\cos\alpha)\right.$$
$$\bullet P_{2i}(\cos\theta)+\sum_{i=1}^{\infty}\left(\frac{-(4i+1)(2i+5)+4(4i+1)\nu}{4i(2i+1)(4i^2+2i+1)+4i(2i+1)(4i+1)\nu}\left(\frac{r}{R}\right)^{2i}+\frac{(4i+1)(4i^2+4n-1)+2(4i+1)\nu}{4i(4i^2-1)(4i^2+2i+1)+4i(4i+1)(4i^2-1)\nu}\left(\frac{r}{R}\right)^{2i-2}\right)\bullet(1+\cos\alpha)$$
$$\left.\bullet P'_{2i}(\cos\alpha)\bullet\frac{\partial^2 P_{2i}(\cos\theta)}{\partial\theta^2}\right] \tag{A1}$$

$$\tilde{\sigma}_\phi = -\frac{1}{2}\left[1 + \sum_{i=1}^{\infty}\left(\frac{-(4i+1)(i-1) + (4i+1)^2\nu}{2i(4i^2+2i+1)+2i(4i+1)\nu}\left(\frac{r}{R}\right)^{2i} + \frac{(4i+1)(4i^2+4n-1)+2(4i+1)\nu}{2(4i^2-1)(4i^2+2i+1)+2(4i+1)(4i^2-1)\nu}\left(\frac{r}{R}\right)^{2i-2}\right)\bullet(1+\cos\alpha)\bullet P'_{2i}(\cos\alpha)\right.$$
$$\bullet P_{2i}(\cos\theta) + \sum_{i=1}^{\infty}\left(\frac{-(4i+1)(2i+5)+4(4i+1)\nu}{4i(2i+1)(4i^2+2i+1)+4i(2i+1)(4i+1)\nu}\left(\frac{r}{R}\right)^{2i} + \frac{(4i+1)(4i^2+4n-1)+2(4i+1)\nu}{4i(4i^2-1)(4i^2+2i+1)+4i(4i+1)(4i^2-1)\nu}\left(\frac{r}{R}\right)^{2i-2}\right)\bullet(1+\cos\alpha)$$
$$\left.\bullet P'_{2i}(\cos\alpha)\bullet\cot\theta\bullet\frac{\partial P_{2i}(\cos\theta)}{\partial\theta}\right] \tag{A2}$$

$$\tilde{\sigma}_r = -\frac{1}{2}\left[1 + \frac{1}{1-\cos\alpha}\sum_{i=1}^{\infty}\frac{2(1+\nu)(1-2\nu)(4i+1)(\cos\alpha\bullet P_{2i}(\cos\alpha) - P_{2i-1}(\cos\alpha))}{(8i^2+8i+3)2\nu+(8i^2+4i+2)(1-2\nu)}\right.$$
$$\left.\bullet\left(\frac{(4i^2-2i-3)\nu}{(1+\nu)(1-2\nu)}\left(\frac{r}{R}\right)^{2i} + \frac{(2i+1)(2i-2)}{2(1+\nu)}\left(\frac{r}{R}\right)^{2i} - \frac{4i^2(2i+2)\nu}{(2i+1)(1+\nu)(1-2\nu)}\left(\frac{r}{R}\right)^{2i-2} - \frac{2i(4i^2+4i-1)}{2(2i+1)(1+\nu)}\left(\frac{r}{R}\right)^{2i-2}\right)\bullet P_{2i}(\cos\theta)\right] \tag{A3}$$

$$\tilde{\tau}_{r\theta} = -\frac{1}{2}\sum_{i=1}^{\infty}\frac{-(4i+1)(4i^2+4i-1)-2(4i+1)\nu}{4i(2i+1)(4i^2+2i+1)+4i(2i+1)(4i+1)\nu}\bullet\left(\left(\frac{r}{R}\right)^{2i} - \left(\frac{r}{R}\right)^{2i-2}\right)\bullet(1+\cos\alpha)\bullet P'_{2i}(\cos\alpha)\bullet\frac{\partial P_{2i}(\cos\theta)}{\partial\theta} \tag{A4}$$

with

$$\alpha = \frac{\arccos(1-2(a/R)^2)}{2} \tag{A5}$$

where ν denotes the Poisson ratio of the (linear elastic) sphere material and $P_{2i}(\cos\theta)$ denotes the Legendre polynomial of degree 2i. The derivative $P'_{2i}(\cos\alpha)$ is defined as

$$P'_{2i}(\cos\alpha) = \frac{\partial P_{2i}(\cos\alpha)}{\partial\cos\alpha} = \frac{P_{2i}(\cos\alpha)}{(-1)(\sin^2\alpha)^{1/2}} \tag{A6}$$

The first and second partial derivatives of the Legendre polynomials $P_{2i}(\cos\theta)$ with respect to θ can be simplified as follows:

$$\frac{\partial P_{2i}(\cos\theta)}{\partial\theta} = \frac{[(-1-2i)\cos\theta P_{2i}(\cos\theta) + (1+2i)P_{2i+1}(\cos\theta)]\bullet\sin\theta}{\sin^2\theta} \tag{A7}$$

$$\frac{\partial^2 P_{2i}(\cos\theta)}{\partial\theta^2} = -\cos\theta\left(\frac{P_{2i}(\cos\theta)}{(-1)(\sin^2\theta)^{1/2}}\right) + \sin^2\theta\left(\frac{P^2_{2i}(\cos\theta)}{(-1)^2(\sin^2\theta)}\right) \tag{A8}$$

where P^2_{2i} is associated Legendre polynomial of degree 2i and of order 2.

The stress tensor coefficients, Eqs. (A1-A4) are given in the form of an infinite series, which has to be truncated. *Mathematica* v. 10.1 (Wolfram Research Inc., Champaign, Illinois) was used to perform summations to p terms and to calculate the stress quantities of interest. Along the sphere vertical axis, where $\cos\theta=1$, the expressions in Eqs. (A1) to (A4) yield an indeterminate solution; hence for simplicity the axis was represented in calculations by using numerical value of $\theta=0.001$ as $|\sigma_1|_{\theta=0} = \lim_{\theta\to 0}\sigma_1$. Likewise, the center of the sphere is defined here as $(\theta, r/R) = (0.001, 0.001)$. With very low relative contact radii a/R and especially for the stress components along the surface ($r/R = 1$), convergence is achieved for relatively high numbers of summation terms p. For example, in the center of the sphere for $(a/R) = 0.1$ the convergence or in other words the result with relative error smaller than 1% is obtained for as few as 10 summations, whereas along the surface near the equator for the same relative contact a relative error below 1% is obtained only for 1000 or more summation terms. In order to compute the stresses along the surface close to the contact perimeter along the θ direction, where the stress peaks for very small contacts below $(a/R) = 0.3$, as many as 100,000 summations had to be used due to the highly oscillatory nature of the expression. This produced near-perimeter stress values with an estimated relative error below 5%.

Appendix. B

See Table B1.

Table B1
Experimental and numerical data of tested particles.

Substrate	Particle #	R [μm]	a/R [μm]	F_{max} [N]	σ_{1c} [MPa]	σ_{1s} [MPa]	Substrate	Particle #	R [μm]	a/R [μm]	F_{max} [N]	σ_{1c} [MPa]	σ_{1s} [MPa]
HV950-#1	1	14.6	0.58 ± 0.02	2.14	1160	960	HV600-#4	1	15.4	0.80 ± 0.02	3.28	270	870
	2	13.1	0.56 ± 0.02	1.53	1100	880		3	12.7	0.74 ± 0.02	1.85	580	860
	4	17.2	0.56 ± 0.01	2.69	1120	900		4	15.6	0.63 ± 0.02	2.13	860	800
	5	30.7	0.47 ± 0.01	6.19	990	700		5	15.7	0.70 ± 0.02	2.55	710	840
	6	12.8	0.56 ± 0.02	1.47	1110	890		6	16.9	0.67 ± 0.02	2.62	740	790
HV950-#2	1	11.9	0.52 ± 0.02	1.17	1120	840		7	14.3	0.90 ± 0.02	3.51	−740	590
	2	12.6	0.56 ± 0.02	1.52	1180	950		9	15.6	0.87 ± 0.02	3.70	−340	690
	3	11.9	0.55 ± 0.02	1.53	1360	1070		10	13.8	0.81 ± 0.02	2.72	200	870
	4	19.2	0.55 ± 0.01	3.43	1170	920	HV600-#5	2	14.6	0.76 ± 0.02	2.48	470	830
	5	11.1	0.56 ± 0.02	1.24	1240	990		3	13.9	0.81 ± 0.02	2.51	180	800
HV750-#1	1	11.4	0.67 ± 0.02	1.49	940	990		4	16.1	0.81 ± 0.02	3.33	180	790
	2	13.6	0.68 ± 0.02	2.19	920	1000		5	14.1	0.93 ± 0.02	3.38	−1110	350
	3	10.9	0.71 ± 0.02	1.61	870	1080		6	17.2	0.61 ± 0.01	1.87	670	590
	8	17.1	0.61 ± 0.02	2.85	1020	900		7	16.9	0.79 ± 0.02	3.45	300	800
HV750-#2	1	14.2	0.70 ± 0.02	2.59	880	1040		8	20.2	0.52 ± 0.01	1.93	640	480
	2	16.6	0.59 ± 0.02	2.29	930	790		9	14.7	0.71 ± 0.02	1.98	590	730
	3	15.4	0.58 ± 0.02	1.88	920	770	HV450-#2	1[a]	20.9	1	–	–	–
	4	19.5	0.52 ± 0.01	2.56	910	680		2[a]	24.0	1	–	–	–
	5	12.9	0.53 ± 0.02	1.12	890	680		3	11.2	0.67 ± 0.02	0.8	520	550
	6	12.8	0.61 ± 0.02	1.49	960	850		5[a]	14.3	1	–	–	–
	7	21.8	0.59 ± 0.01	4.16	980	830		6	16.3	0.62 ± 0.02	1.56	590	540
	8	15.5	0.58 ± 0.02	1.95	940	780		7[a]	11.8	1	–	–	–
	9	13.8	0.59 ± 0.02	1.48	870	740		8[a]	17.5	1	–	–	–
	10	17.7	0.51 ± 0.01	1.77	780	580	HV450-#3	1[a]	11.3	1	–	–	–
	11	13.3	0.54 ± 0.02	1.09	790	610		2[a]	16.2	1	–	–	–
	13	27.7	0.53 ± 0.01	4.52	780	600		5[a]	16.5	1	–	–	–
HV750-#3	1	18.5	0.55 ± 0.01	2.49	910	720		6[a]	14.3	1	–	–	–
	3	16.2	0.68 ± 0.02	3.08	910	1000		8[a]	17.5	1	–	–	–
	4	13.4	0.68 ± 0.02	2.12	910	990	HV450-#4	1	13.2	0.53 ± 0.02	0.78	590	450
	5	17.5	0.64 ± 0.01	3.13	950	910		3[a]	17.7	1	–	–	–
	6	16.8	0.61 ± 0.02	2.81	1050	930		4	14.4	0.82 ± 0.02	2.12	85	600
	7	12.8	0.63 ± 0.02	1.61	960	900		5	12.1	0.68 ± 0.02	1.05	560	610
	8	13.9	0.66 ± 0.02	2.25	990	1010		6[a]	16.8	1	–	–	–
	9	16.3	0.66 ± 0.02	3.00	970	980		7[a]	13.3	1	–	–	–
	10	14.9	0.61 ± 0.02	2.2	1040	920	HV450-#5	1[a]	13.2	1	–	–	–
HV600-#1	1	12.2	0.82 ± 0.02	2.03	110	810		2[a]	18.5	1	–	–	–
	2	16.4	0.39 ± 0.02	0.7	440	290		3[a]	13.9	1	–	–	–
	3	21.9	0.57 ± 0.01	2.88	720	580		4[a]	13.9	1	–	–	–
	4	12.5	0.39 ± 0.02	0.4	440	290		5	22.6	0.44 ± 0.01	1.37	430	290
	5	11.6	0.81 ± 0.02	2.02	210	920		6	22.2	0.65 ± 0.01	3.1	560	550
	6	14.4	0.73 ± 0.02	2.43	640	900		7[a]	13.2	1	–	–	–
	7	14.7	0.31 ± 0.02	0.38	330	200							
	9	16	0.68 ± 0.02	2.69	810	890							
	11	15.5	0.62 ± 0.02	1.82	770	700							

[a] Particle embedded completely with no failure detected.

Appendix. C

Fig. C1 summarizes a static fatigue test in which a particle was loaded and held for several seconds under constant load until failure was detected. This demonstrates that slow crack growth is operative in the particles under conditions of the present tests. In Fig. C2 we show optical and SEM images of four particles, which contained apparent internal defects.

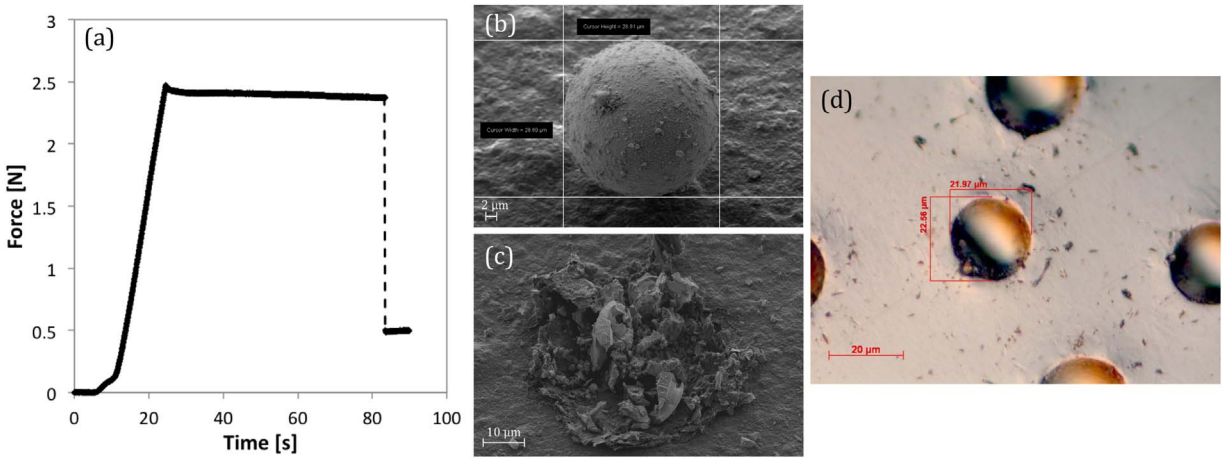

Fig. C1. The uniaxial compression test done in the same conditions as the other test in this work except that loading was deliberately interrupted before failure and particle was left under the static load of roughly 2.5 N with the relative contact radius of ~0.87 resulting in roughly 600 MPa peak surface stress for approximately 60 s after which the particle failure occurred accompanied by a sharp drop in load. The particle failed in shattering mode into many pieces as was typical for the majority of particles tested in the study. This experiment shows that particle may fail even after the maximum attainable peak tensile surface stress was applied when SCG operates.

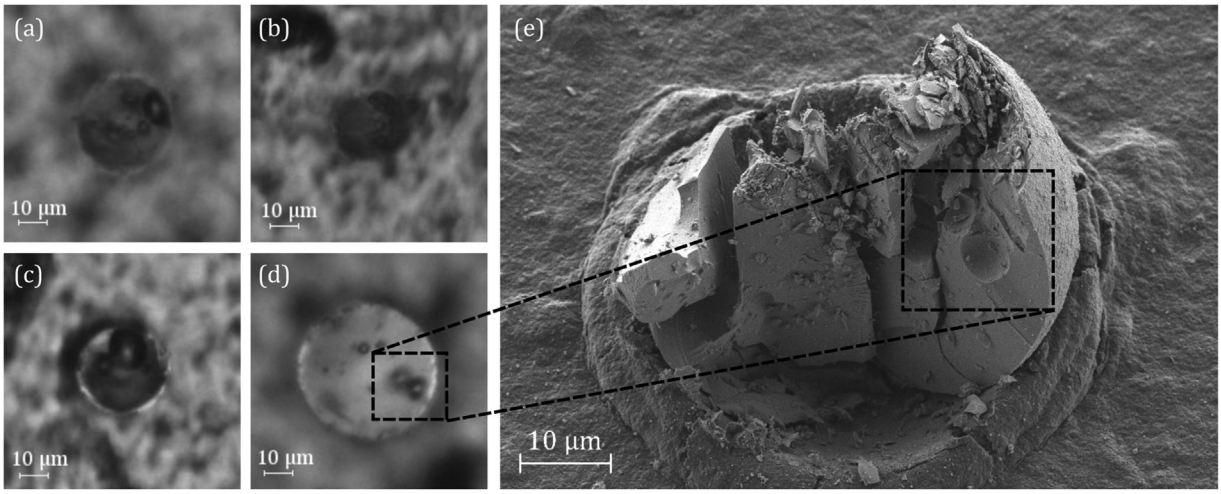

Fig. C2. Particles with apparent internal pores that were not considered in the surface failure statistics. (a), (b), (c), (d) optical images before the test of particles HV600-#1–2, HV600-#1–4, HV600-#1–7 and HV450-#5-5, respectively. (e) SEM image made at 33° tilt after the test of the particle A564-AH-450-#5-5 with two big pores present on the fracture surface that match the two distinct dark spots on the optical image.

Appendix. D

Using the computational software *Mathematica* 10.1 we show here on a hypothetical sample that when both the surface and the center strength are Weibull-distributed and the two are independent, then if one applies the left-truncation, right-censoring survival analysis scheme and the testing method exposed in the main body text, then the obtained distribution converges to the pre-defined surface strength distribution.

Assume that the surface strength and strength in the particle center are Weibull distributed. Let us first generate 3 random samples from the predefined Weibull distribution of the surface strength and 3 random samples from the Weibull distribution of the center strength, keeping the two at equal length. Let the Weibull distribution of the surface strength have shape parameter m =7 and scale parameter s=900, then three random sample examples are:

{845, 1048, 872, 1059, 797, 719, 521, 879, 829, 1165, 1072, 943, 639, 970, 1081, 670, 944, 794, 900, 903, 905, 971, 679, 939, 861, 848, 801, 733, 1001, 560}.

{768, 860, 894, 846, 952, 830, 464, 725, 843, 582, 960, 693, 774, 912, 853, 459, 1017, 530, 735, 847, 784, 963, 708, 920, 995, 636, 957, 779, 925, 1038}.

{743, 834, 989, 965, 789, 713, 1018, 1010, 913, 804, 961, 766, 743, 752, 844, 600, 836, 1001, 842, 804, 854, 863, 1034, 874, 706, 775, 919, 898, 1038, 1037}.

Take the Weibull distribution of the center strength to have shape parameter m =3 and scale parameter s=1300, then three random samples of equal length as for the surface strength are.

{1099, 2026, 895, 1132, 1630, 869, 1322, 1353, 1907, 1812, 605, 1388, 1600, 1121, 1066, 1046, 1487, 1718, 1439, 1656, 940, 1199, 1124, 1859, 1479, 1471, 835, 983, 1594, 826}.

{590, 1102, 2077, 2194, 1666, 1258, 1820, 846, 1659, 1210, 1012, 1139, 1291, 534, 1667, 1365, 1574, 1441, 609, 607, 583, 1534, 971, 790, 1009, 1502, 1478, 1284, 1487, 773}.

{984, 1408, 1089, 1534, 862, 1177, 1257, 1884, 407, 1305, 1100, 1687, 948, 1097, 811, 936, 1192, 1355, 1102, 1893, 628, 1476, 1632, 1215, 2084, 2186, 619, 282, 1683, 1977}.

We can now join three random samples of surface strength with those of central strength and form three sets of duplets. In each duplet the first number represent the surface strength and the second the center strength. Thus each duplet can be seen as a particle (colors are explained in the next paragraph):

{**{845, 1099}**, **{1048, 2026}**, **{872, 895}**, **{1059, 1132}**, **{797, 1630}**, **{719, 869}**, ***{521, 1322}***, **{879, 1353}** , **{829, 1907}**, **{1165, 1812}**, **{1072, 605}**, **{943, 1388}**, {639, 1600}, **{970, 1121}**, **{1081, 1066}**, **{670, 1046}**, **{944, 1487}**, **{794, 1718}**, **{900, 1439}**, **{903, 1656}**, **{905, 940}**, **{971, 1199}**, **{679, 1124}**, **{939, 1859}**, **{861, 1479}**, **{848, 1471}**, **{801, 835}**, **{733, 983}**, **{1001, 1594}**, {560, 826}}.

{*{768, 590}*, {860, 1102}, {894, 2077}, {846, 2194}, **{952, 1666}**, {830, 1258}, ***{464, 1820}***, {725, 846}, {843, 1659}, ***{582, 1210}***, **{960, 1012}**, ***{693, 1139}***, {774, 1291}, *{912, 534}*, {853, 1667}, ***{459, 1365}***, **{1017, 1574}**, ***{530, 1441}***, *{735, 609}*, *{847, 607}*, *{784, 583}*, **{963, 1534}**, {708, 971}, *{920, 790}*, **{995, 1009}**, ***{636, 1502}***, **{957, 1478}**, {779, 1284}, **{925, 1487}**, *{1038, 773}*}.

{*{743, 984}*, ***{834, 1408}***, {989, 1089}, {965, 1534}, *{789, 862}*, ***{713, 1177}***, {1018, 1257}, {1010, 1884}, *{913, 407}*, ***{804, 1305}***, {961, 1100}, ***{766, 1687}***, *{743, 948}*, ***{752, 1097}***, *{844, 811}*, *{600, 936}*, ***{836, 1192}***, {1001, 1355}, ***{842, 1102}***, ***{804, 1893}***, *{854, 628}*, ***{863, 1476}***, {1034, 1632}, ***{874, 1215}***, ***{706, 2084}***, ***{775, 2186}***, *{919, 619}*, *{898, 282}*, {1038, 1683}, {1037, 1977}}.

Let us now consider that a first set of the particles (or duplets) is tested with platen material 1 (Platen 1), a second set with platen material 2 (Platen 2) and the third (remaining) set with platen material 3 (Platen 3). Platen 1 is such that, during the test, a particle will be stressed in the center up to maximum of 600 (say, MPa; however, units are abitrary). Platen 2 will stress the center of a particle up to 800 and Platen 3 will stress a particle up to 1000 before the stress in center starts to decrease (transition from Domain

Table D1
Data from a hypothetical test.

Platen	Failure/censoring peak surface stress [MPa]	Censoring indicator[a]	Left-truncated at [MPa]	Platen	Failure/ censoring peak surface stress [MPa]	Censoring indicator[a]	Left-truncated at [MPa]
Platen 1	650	1	550	Platen 2	860	0	700
	650	1	550		894	0	700
	650	1	550		846	0	700
	650	1	550		900	1	700
	650	1	550		830	0	700
	650	1	550		725	0	700
	650	1	550		843	0	700
	650	1	550		900	1	700
	650	1	550		774	0	700
	650	1	550		853	0	700
	650	1	550		900	1	700
	639	0	550		900	1	700
	650	1	550		708	0	700
	650	1	550		900	1	700
	650	1	550		900	1	700
	650	1	550		779	0	700
	650	1	550		900	1	700
	650	1	550	Platen 3	989	0	900
	650	1	550		965	0	900
	650	1	550		1018	0	900
	650	1	550		1010	0	900
	650	1	550		961	0	900
	650	1	550		1001	0	900
	650	1	550		1034	0	900
	650	1	550		1038	0	900
	650	1	550		1037	0	900
	650	1	550				
	650	1	550				
	560	0	550				

[a] when 0, the peak surface stress represents the surface strength measurement, otherwise value 1 indicates righ-censoring and the peak surface stress represents lower-bound of the surface strength.

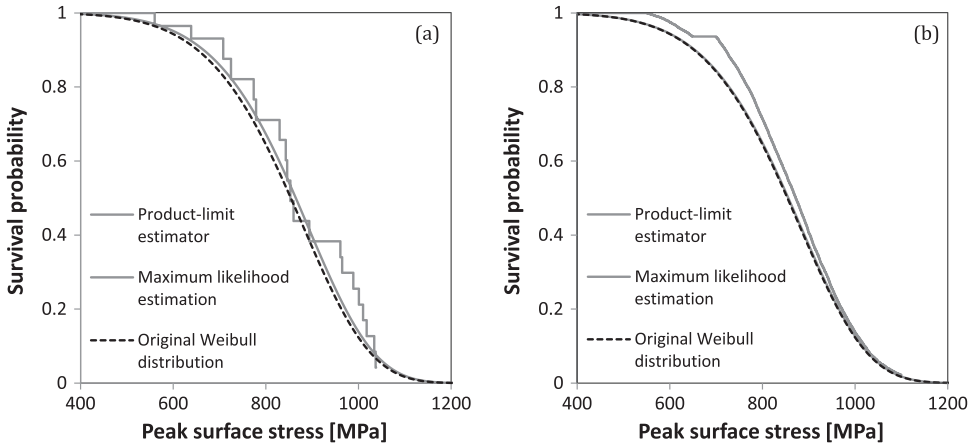

Fig. D1. (a) Product-limit estimator of the left-truncated and right-censored data from the Tab. D1 obtained from hypothetical three sets of 30 duplets representing particles tested in the Meridian crack test along with the Maximum likelihood estimation of two parameter Weibull distribution (m =7.2, s=910). (b) Product-limit estimator of the left-truncated and right-censored obtained from hypothetical three sets of 10,000 duplets representing particles tested in the Meridian crack test along with the Maximum likelihood estimation of two-parameter Weibull distribution (m =7.01, s=902). In both cases the original Weibull distribution of surface strength was with parameters m =7, s=900.

II to Domain III).

Under those circumstances, all particles that are tested with Platen 1 and have a strength in their center (second number in duplets) lower than 600 will break before the relative contact radius reaches Domain III, in which one knows that failure is caused by a surface flaw. Let us remove for now those particles from consideration and let us also do so for corresponding values of the other two platens. We thus eliminate for now from consideration all duplets that (i) for Platen 1 (Set 1) have central strength lower than 600 (ii) for Platen 2 (Set 2) have central strength lower than 800 and (iii) for Platen 3 (Set 3) have central strength lower than 1000. Such cases are written in italics in the list above.

Next, the test is designed such that only particles that enter Domain III are those that "we know" broke by meridian cracking due to a flaw located along their surface. Let the surface stress applied to the particle at the beginning of Domain III be (i) 550 for Platen 1 (ii) 700 for Platen 2 and (iii) 900 for Platen 3. We label therefore those particles (duplets) that will break due to surface failure before reaching Domain III in bold and italics font. All particles that are now labeled in italics or bold and italics will fail, whether due to center or surface flaws, before reaching Domain III. The surface stress levels at the beginning of Domain III for each platen also represent the left-truncation in the following survival analysis.

Some particles will not break and will rather embed completely, producing right-censored data. Let the maximum applied surface stress during a test be (i) 650 for Platen 1 (ii) 900 for Platen 2 and (iii) 1100 for Platen 3. We label particles that have a surface strength higher than the maximum attainable surface strength for a given platen in bold.

Remaining (unformatted text) particles are ones that will break in Domain III; there are 2+10+9=21 such valid surface strength measurements, and 27+7+0=34 right-censored data that entered Domain IV. Now, if we consider all these Domain III and IV data to be left-truncated at (i) 550 for Platen 1 (ii) 700 for Platen 2 and (iii) 900 for Platen 3 we obtain from the test the data present in Table D1 for the particle surface strength.

If we now apply the product-limit estimator using the *Mathematica* built-in function *SurvivalModelFit* on the data from Table D1 we get the result plotted in Fig. D1a. The estimated Weibull distribution using the maximum likelihood method via the *Mathematica* built-in function *EstimatedDistribution* is m =7.2 and s=910 (the original values were m =7 and s=900). The same procedure can be applied also for much larger sample sizes, for example with 10 000 random variate duplets for each platen. The result is shown in Fig. D1b. As can be seen the Maximum likelihood estimation converges to the original distribution (estimated parameters m =7.01 and s=902), while the Product-limit estimator is somewhat inaccurate for low surface strength values (this is caused by the fact that the data are truncated at 550 therefore cannot be precise around that value). On the other hand the Product-limit estimator does not require any assumption on the nature of the surface strength distribution.

Appendix E. Supporting information

Supplementary data associated with this article can be found in the online version at http://dx.doi.org/10.1016/j. jmps.2016.11.009.

References

Antonyuk, S., Heinrich, S., Tomas, J., Deen, N.G., van Buijtenen, M.S., Kuipers, J.A.M., 2010. Energy absorption during compression and impact of dry elastic-plastic spherical granules. Granul. Matter 12, 15–47. http://dx.doi.org/10.1007/s10035-009-0161-3.

Antonyuk, S., Tomas, J., Heinrich, S., Mörl, L., 2005. Breakage behaviour of spherical granulates by compression. Chem. Eng. Sci. 60, 4031–4044. http://dx.doi.org/10.1016/j.ces.2005.02.038.
Armstrong, J.L., Matthewson, M.J., Kurkjian, C.R., 2000. Humidity Dependence of the Fatigue of High-Strength Fused Silica Optical Fibers. J. Am. Ceram. Soc. 83, 3100–3109. http://dx.doi.org/10.1111/j.1151-2916.2000.tb01689.x.
Balakrishnan, N., Mitra, D., 2012. Left truncated and right censored Weibull data and likelihood inference with an illustration. Comput. Stat. Data Anal. 56, 4011–4025. http://dx.doi.org/10.1016/j.csda.2012.05.004.
Broch, E., Franklin, J.A., 1972. The point-load strength test. Int. J. Rock. Mech. Min. Sci. Geomech. Abstr. 9, 669–676. http://dx.doi.org/10.1016/0148-9062(72)90030-7.
Brzesowsky, R.H., Spiers, C.J., Peach, C.J., Hangx, S.J.T., 2011. Failure behavior of single sand grains: theory versus experiment. J. Geophys. Res., 116. http://dx.doi.org/10.1029/2010JB008120.
Chaudhri, M.M., 2004. Impact breakage of semi-brittle spheres. Powder Technol. Part. Break. 143–144, 31–40. http://dx.doi.org/10.1016/j.powtec.2004.04.006.
Chau, K.T., Wei, X.X., Wong, R.H.C., Yu, T.X., 2000. Fragmentation of brittle spheres under static and dynamic compressions: experiments and analyses. Mech. Mater. 32, 543–554. http://dx.doi.org/10.1016/S0167-6636(00)00026-0.
Darvell, B.W., 1990. Uniaxial compression tests and the validity of indirect tensile strength. J. Mater. Sci. 25, 757–780.
Dean, W.R., Sneddon, I.M., Parsons, H.W., 1952. Distribution of Stress in a Decelerating Elastic Sphere (No. 29), Selected Government Reasearch Reports: Strengthstrength and Testing of Materials: Partpart Ii: Testingtesting Methods and Test Results. H. Majesty's Stationery Office, London.
Dieter, G.E., 1986. Mechanical Metallurgy, Mcgraw-hill Series in Materials Science and Engineering. 3rd ed.. McGraw-Hill, New York.
Evans, A.G., Johnson, H., 1975. The fracture stress and its dependence on slow crack growth. J. Mater. Sci. 10, 214–222. http://dx.doi.org/10.1007/BF00540345.
Gammage, J., Wilkinson, D., Brechet, Y., Embury, D., 2004. A model for damage coalescence in heterogeneous multi-phase materials. Acta Mater. 52, 5255–5263. http://dx.doi.org/10.1016/j.actamat.2004.07.009.
Gerberich, W.W., Mook, W.M., Perrey, C.R., Carter, C.B., Baskes, M.I., Mukherjee, R., Gidwani, A., Heberlein, J., McMurry, P.H., Girshick, S.L., 2003. Superhard silicon nanospheres. J. Mech. Phys. Solids 51, 979–992. http://dx.doi.org/10.1016/S0022-5096(03)00018-8.
Hauert, A., Rossoll, A., Mortensen, A., 2009. Ductile-to-brittle transition in tensile failure of particle-reinforced metals. J. Mech. Phys. Solids 57, 473–499. http://dx.doi.org/10.1016/j.jmps.2008.11.006.
Hiramatsu, Y., Oka, Y., 1967. Determination of the tensile strength of rock by a compression test of an irregular test piece: authors' reply to discussion by. J. Salençon. Int. J. Rock. Mech. Min. Sci. Geomech. Abstr. 4, 363–365. http://dx.doi.org/10.1016/0148-9062(67)90017-4.
Hiramatsu, Y., Oka, Y., 1966. Determination of the tensile strength of rock by a compression test of an irregular test piece. Int. J. Rock. Mech. Min. Sci. Geomech. Abstr. 3, 89–99. http://dx.doi.org/10.1016/0148-9062(66)90002-7.
Huang, J., Xu, S., Yi, H., Hu, S., 2014. Size effect on the compression breakage strengths of glass particles. Powder Technol. 268, 86–94. http://dx.doi.org/10.1016/j.powtec.2014.08.037.
Hull, D., 1999. Fractography: observing, Measuring and Interpreting Fracture Surface Topography. Cambridge University Press, Cambridge.
Jaeger, J.C., 1967. Failure of rocks under tensile conditions. Int. J. Rock. Mech. Min. Sci. Geomech. Abstr. 4, 219–227. http://dx.doi.org/10.1016/0148-9062(67)90046-0.
Kaplan, E.L., Meier, P., 1958. Nonparametric Estimation from Incomplete Observations. J. Am. Stat. Assoc. 53, 457. http://dx.doi.org/10.2307/2281868.
Kelly, E.G., Spottiswood, D.J., 1990. The breakage function; What is it really? Miner. Eng. 3, 405–414. http://dx.doi.org/10.1016/0892-6875(90)90034-9.
Khanal, M., Schubert, W., Tomas, J., 2008. Compression and impact loading experiments of high strength spherical composites. Int. J. Miner. Process. 86, 104–113. http://dx.doi.org/10.1016/j.minpro.2007.12.001.
Kiener, D., Motz, C., Rester, M., Jenko, M., Dehm, G., 2007. FIB damage of Cu and possible consequences for miniaturized mechanical tests. Mater. Sci. Eng. A 459, 262–272. http://dx.doi.org/10.1016/j.msea.2007.01.046.
Klein, J.P., Moeschberger, M.L., 2003. Survival analysis: techniques for censored and truncated dataStatistics for biology and health 2nd ed. Springer, New York.
Lawn, B.R., 1993. Fracture of brittle solids (ed)Cambridge solid state science series 2nd ed.. Cambridge University Press, Cambridge New York.
Lobo-Guerrero, S., Vallejo, L.E., 2006. Application of Weibull statistics to the tensile strength of rock aggregates. J. Geotech. Geoenviron. Eng. 132, 786–790. http://dx.doi.org/10.1061/(ASCE)1090-0241(2006)132:6(786).
Majzoub, R., Chaudhri, M.M., 2000. High-speed photography of low-velocity impact cracking of solid spheres. Philos. Mag. Lett. 80, 387–393. http://dx.doi.org/10.1080/095008300403521.
McDowell, G.R., Amon, A., 2000. The application of Weibull statistics to the fracture of soil particles. J. Jpn. Geotech. Soc. Soils Found. 40, 133–141.
McDowell, G.R., Bolton, M.D., 1998. On the micromechanics of crushable aggregates. Géotechnique 48, 667–679. http://dx.doi.org/10.1680/geot.1998.48.5.667.
Miserez, A., Mortensen, A., 2004. Fracture of aluminium reinforced with densely packed ceramic particles: influence of matrix hardening. Acta Mater. 52, 5331–5345. http://dx.doi.org/10.1016/j.actamat.2004.07.038.
Mook, W.M., Nowak, J.D., Perrey, C.R., Carter, C.B., Mukherjee, R., Girshick, S.L., McMurry, P.H., Gerberich, W.W., 2007. Compressive stress effects on nanoparticle modulus and fracture. Phys. Rev. B, 75. http://dx.doi.org/10.1103/PhysRevB.75.214112.
Mueller, M.G., Pejchal, V., Žagar, G., Singh, A., Cantoni, M., Mortensen, A., 2015. Fracture toughness testing of nanocrystalline alumina and fused quartz using chevron-notched microbeams. Acta Mater. 86, 385–395. http://dx.doi.org/10.1016/j.actamat.2014.12.016.
Nakata, Y., Hyde, A.F.L., Hyodo, M., Murata, H., 1999. A probabilistic approach to sand particle crushing in the triaxial test. Géotechnique 49, 567–583. http://dx.doi.org/10.1680/geot.1999.49.5.567.
Ogiso, H., Yoshida, M., Nakano, S., Akedo, J., (2007). Effects of Al ion implantation on the strength of Al2O3 particles. Surf. Coat. Technol. In: Proceedings of the SMMIB 2005 14th International Conference on Surface Modification of Materials by Ion Beams 201, 8180–8184. doi:10.1016/j.surfcoat.2006.01.093
Oka, Y., Majima, H., 1970. A theory of size reduction involving fracture mechanics. Can. Metall. Q. Can. J. Metall. Mater. Sci. 9, 429–439. http://dx.doi.org/10.1179/cmq.1970.9.2.429, (Y).
Pitchumani, R., Zhupanska, O., Meesters, G.M.H., Scarlett, B., 2004. Measurement and characterization of particle strength using a new robotic compression tester. Powder Technol. 143–144, 56–64. http://dx.doi.org/10.1016/j.powtec.2004.04.007.
Portnikov, D., Kalman, H., Aman, S., Tomas, J., 2013. Investigating the testing procedure limits for measuring particle strength distribution. Powder Technol. 237, 489–496. http://dx.doi.org/10.1016/j.powtec.2012.12.025.
Proctor, B.A., Whitney, I., Johnson, J.W., 1967. The strength of fused silica. Proc. R. Soc. Lond. Math. Phys. Eng. Sci. 297, 534–557. http://dx.doi.org/10.1098/rspa.1967.0085.
Ribas, L., Cordeiro, G.C., Toledo Filho, R.D., Tavares, L.M., 2014. Measuring the strength of irregularly-shaped fine particles in a microcompression tester. Miner. Eng. 65, 149–155. http://dx.doi.org/10.1016/j.mineng.2014.05.021.
Rice, R.W., 1979. Machining Flaws and the Strength Grain Size Behavior of Ceramics. In: The Science of Ceramic Machining and Surface Finishing II. Presented at the The Science of Ceramic Machining and Surface Finishing II. National Bureau of Standards Special Publication, Gaithensburg, Maryland, 429–454.
Romeis, S., Paul, J., Ziener, M., Peukert, W., 2012. A novel apparatus for in situ compression of submicron structures and particles in a high resolution SEM. Rev. Sci. Instrum. 83, 095105. http://dx.doi.org/10.1063/1.4749256.
Rozenblat, Y., Portnikov, D., Levy, A., Kalman, H., Aman, S., Tomas, J., 2011. Strength distribution of particles under compression. Powder Technol. 208, 215–224. http://dx.doi.org/10.1016/j.powtec.2010.12.023.
Salem, J.A., 2013. Transparent Armor Ceramics as Spacecraft Windows. J. Am. Ceram. Soc. 96, 281–289. http://dx.doi.org/10.1111/jace.12089.
Salençon, J., 1966. Comments on "determination of the tensile strength of rock by a compression test of an irregular test piece. Int. J. Rock. Mech. Min. Sci. Geomech. Abstr. 3, 349–350.
Schönert, K., 2004. Breakage of spheres and circular discs. Powder Technol., 143–144. http://dx.doi.org/10.1016/j.powtec.2004.04.004.
Shim, S., Bei, H., Miller, M.K., Pharr, G.M., George, E.P., 2009. Effects of focused ion beam milling on the compressive behavior of directionally solidified micropillars and the nanoindentation response of an electropolished surface. Acta Mater. 57, 503–510. http://dx.doi.org/10.1016/j.actamat.2008.09.033.
Shipway, P.H., Hutchings, I.M., 1993a. Fracture of brittle spheres under compression and impact loading. I. Elastic stress distributions. Philos. Mag. A 67,

1389–1404. http://dx.doi.org/10.1080/01418619308225362.
Shipway, P.H., Hutchings, I.M., 1993b. Fracture of brittle spheres under compression and impact loading. II. Results for lead-glass and sapphire spheres. Philos. Mag. A 67, 1405–1421. http://dx.doi.org/10.1080/01418619308225363.
Suratwala, T.I., Steele, R.A., 2003. Anomalous temperature dependence of sub-critical crack growth in silica glass. J. Non-Cryst. Solids 316, 174–182. http://dx.doi.org/10.1016/S0022-3093(02)01799-4.
Swab, J.J., Yu, J., Gamble, R., Kilczewski, S., 2011. Analysis of the diametral compression method for determining the tensile strength of transparent magnesium aluminate spinel. Int. J. Fract. 172, 187–192. http://dx.doi.org/10.1007/s10704-011-9655-1.
Tabor, D., 1951. The Hardness of Metals, Monographs on the physics and chemistry of materials. Clarendon Press.
Tavares, L.M., 2007. Chapter 1 Breakage of single particles: quasi-static. In: Salman, A.D., Ghadiri, M., Hounslow, M.J. (Eds.), Handbook of Powder Technology. Elsevier Science B.V., 3–68.
Verrall, R.J., 1976. A sphere compression test for measuring the mechanical properties of dental composite materials. J. Dent. 4, 11–14. http://dx.doi.org/10.1016/0300-5712(76)90064-6.
Wiederhorn, S.M., Bolz, L.H., 1970. Stress corrosion and static fatigue of glass. J. Am. Ceram. Soc. 53, 543–548.
Wijk, G., 1978. Some new theoretical aspects of indirect measurements of the tensile strength of rocks. Int. J. Rock. Mech. Min. Sci. Geomech. Abstr. 15, 149–160. http://dx.doi.org/10.1016/0148-9062(78)91221-4.
Yap, S.F., Adams, M.J., Seville, J.P.K., Zhang, Z., 2008. Single and bulk compression of pharmaceutical excipients: evaluation of mechanical properties. Powder Technol. 185, 1–10. http://dx.doi.org/10.1016/j.powtec.2007.09.005.
Yap, S.F., Adams, M., Seville, J., Zhang, Z., 2006. Understanding the mechanical properties of single micro-particles and their compaction behaviour. China Part. 4, 35–40. http://dx.doi.org/10.1016/S1672-2515(07)60231-0.
Yoshida, M., Ogiso, H., Nakano, S., Akedo, J., 2005. Compression test system for a single submicrometer particle. Rev. Sci. Instrum. 76, 093905. http://dx.doi.org/10.1063/1.2038187.
Žagar, G., Pejchal, V., Mueller, M.G., Michelet, L., Mortensen, A., 2016. Fracture toughness measurement in fused quartz using triangular chevron-notched micro-cantilevers. Scr. Mater. 112, 132–135. http://dx.doi.org/10.1016/j.scriptamat.2015.09.032.
Žagar, G., Pejchal, V., Mueller, M.G., Rossoll, A., Cantoni, M., Mortensen, A., 2015a. The local strength of microscopic alumina reinforcements. Acta Mater. 100, 215–223. http://dx.doi.org/10.1016/j.actamat.2015.08.026.
Žagar, G., Singh, A., Pejchal, V., Mueller, M.G., Mortensen, A., 2015b. On measuring fracture toughness under load control in the presence of slow crack growth. J. Eur. Ceram. Soc. 35, 3155–3166. http://dx.doi.org/10.1016/j.jeurceramsoc.2015.04.004.
Zhao, S., Gan, Y., Kamlah, M., Kennerknecht, T., Rolli, R., 2013. Influence of plate material on the contact strength of Li4SiO4 pebbles in crush tests and evaluation of the contact strength in pebble–pebble contact. Eng. Fract. Mech. 100, 28–37. http://dx.doi.org/10.1016/j.engfracmech.2012.05.011.